Upper Limits for the Photoproduction Cross Section for the $\Phi^{--}(1862)$ Pentaquark State in $\Xi^-\pi^-$ Decay Channel Using EG3 Data

H. Egiyan, M. Holtrop, E. Smith, S. Stepanyan, R. Gothe, J. Langheinrich, M. Ito, G. Mutchler, Zh. Zhao, P. Mattione

January 7, 2009

Abstract

We analyze the entire EG3 data set searching for the $\Phi^{--}(1862)$ pentaquark in the $\Xi^-\pi^-$ decay channel using CLAS. The invariant mass spectra of $\Lambda\pi^-\pi^-$ and $\Xi^-\pi^-$ systems allow us to set limits on the strength of narrow resonant structures near the mass $M = 1.86$ GeV. The analysis of the sideband-subtracted mass spectrum yields a 90% CL upper limit of ~ 450 pb for the photoproduction cross section of $\Phi^{--}(1862)$ with a subsequent decay to $\Xi^-\pi^-$ system in the photon energy range 4.5 GeV $< E_\gamma < 5.5$ GeV.

Contents

1 Introduction

In 1997 Diakonov et.al. [1] predicted the existence of a narrow bound state of four quarks and one anti-quark. The calculation using the Chiral Soliton Model predicted states which were grouped together into an anti-decuplet of baryons. Three of the ten baryons in this anti-decuplet (see Fig. 1) have "exotic" quantum numbers, that is they are not present in the standard quark model. The lightest member, called the Θ^+, was predicted to be narrow (15 MeV) and have a mass of about 1.53 GeV. Initially several experiments reported observations consistent with this new state. However, extended experimental scrutiny has repudiated the original reports to the point that this exotic baryon is no longer listed in the particle summary table by the Particle Data Group [2] .

The two other exotic states in the anti-decuplet have $S = -2$, one with charge $Q = -2$ and the other with $Q = +1$. They are cascades states with $J = 3/2$, in contrast to the normal octet cascades states which have $J = 1/2$. In the literature they are referred to with various notation, including Ξ_5 with the subscript to indicate their 5-quark content. However, the Particle Data Group has assigned the name of $\Phi(1860)$ to this state, where the mass refers to the only experimental observation by NA49 at a mass of 1.862 GeV [3]. This measurement was conducted with p + p collisions at a center-of-mass energy $\sqrt{s}$=17.2 GeV. The two exotic states are Φ^{--} and the Φ^0, and their non-exotic partners are denoted Φ^- and Φ^0. The NA49 collaboration reported evidence for the exotic pentaquark Φ^{--} and the non-exotic Φ^0, which were reconstructed from their decay products using their decays into $\Phi^{--} \to \Xi^-\pi^-$ and $\Phi^0 \to \Xi^-\pi^+$. We note that many experiments [4, 5, 6, 7, 8, 9, 10, 11, 12, 13, 14], some of which represented a much larger statistical sample, have not been able to confirm this observation.

The purpose of this analysis is to search specifically for the $\Phi^{--}(1862)$ of the anti-decuplet with the CLAS detector [15] in a photoproduction experiment. This paper will review the EG3 data analysis performed to look for evidence for any signal in the $\Xi^-(1321)\pi^-$ decay channel and to set an upper limit for photoproduction cross section.

1.1 Mass estimates

Guidance for where and how to search for cascade pentaquarks is very sparse. Most of the models have concentrated on predicting the mass range of these
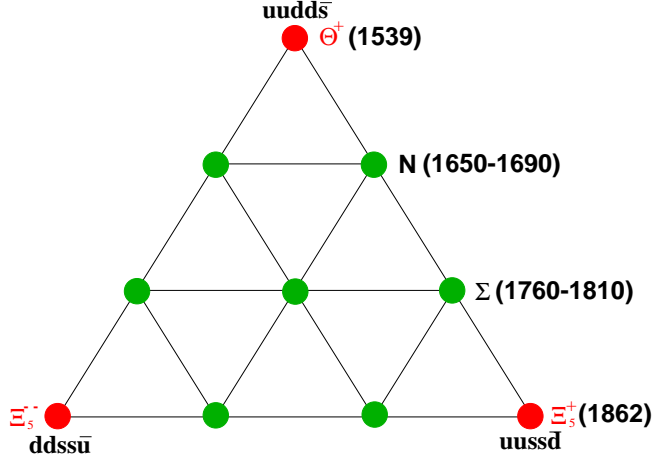
Figure 1: Anti-decuplet predicted by the chiral soliton model [16]. The masses in parenthesis are updated values for the predicted masses. The red corners of the anti-decuplet have exotic quantum numbers. The quark content of the exotic members are also displayed.

particles. Within the quark models, the mass scale for the Θ^+ can be estimated to be about the mass of the nucleon (0.94 GeV) plus the mass of the kaon (0.5 GeV). The mass of the cascade pentaquark contains an additional strange quark (assuming the strange and anti-strange quarks have the same mass of about 0.45 GeV) which gives 1.89 GeV. The quark models predictions vary depending on the amount of mixing between the anti-decuplet and octet members, as well as the estimated size of the color-spin hyperfine interaction between quarks. We also note that many of the models have used the experimental observations of either the Θ^+ or $\Phi(1860)$, or both, to set the scale so are not entirely unbiased. Table 1 summarizes representative model predictions for the masses of the cascade pentaquark which range from 1.75 to 2.07 GeV.

The width of the $\Phi(1860)$ is estimated relative to the width of the Θ^+. In the Chiral-Soliton model [16], the estimated width gives $\Gamma_{\Phi^{--}} \approx 5\Gamma_{\Theta^+}$. In the diquark model [19], the estimated width is $\Gamma_{\Phi^{--}} \approx 3.4\Gamma_{\Theta^+}$.

Source	Reference	Mass (GeV)
Chiral-Soliton Model	Diakonov, Petrov, Polyakov [1, 16]	2.07 [1.86]
Chiral-Soliton Model	Ellis, Karliner, Praszalowicz [17]	1.79-1.97
Diquark Model	Jaffe, Wilczek [18, 19]	1.75
Diquark-Triquark Model	Majee, Raychaudhuri [20, 21]	1.783
Experiment	NA49 [3]	1.862

Table 1: Selected model expectations for the mass of the cascade pentaquark. Note that the first entry gives the initial prediction of the Chiral-Soliton model of 2.07 GeV followed in square brackets with the adjusted model to the experimental value of NA49. This is not a comprehensive list of all model calculations but is very representative.

1.2   Production cross section

There is very limited guidance on the production mechanism or the cross section for production. There is only one calculation of the production cross section of exotic cascades with photon beams [22, 23] which is illustrated in Figs. 2 and 3. The calculations are for $\sigma(\gamma n \rightarrow K^+ K^+ \Xi^{--})$ and for $\sigma(\gamma p \rightarrow K^0 K^0 \Xi^+)$, corresponding to similar reaction channels for the neutron and proton. The calculations are conducted using a model which uses a generalization of the SU(3) flavor-invariant Lagrangian for the interaction between octet pseudoscalar mesons and baryons to include the interactions of the Θ^+ with nucleons and K as well as K* mesons. The predictions off a neutron target are generally larger than off the proton, but uncertainties are very large. The dominant mechanism for production off the neutron is charged K$^+$ exchange, so uncertainties in the $g_{K^*N\Xi}$ coupling constant do not change the predictions very much. Conversely, the production off the proton varies considerably depending on the value of the $g_{K^*N\Xi}$ coupling. At $E_\gamma =$ 5 GeV the estimated $\sigma(\gamma n \rightarrow K^+ K^+ \Xi^{--})$ including effective form factors varies between 0.4 and 1.5 nb depending on the value of the $g_{K^*N\Xi}$ coupling.[1]

As an aside, we note that additional pions could be produced along with the cascade pentaquark. However, as these measurements are performed near threshold, additional particles will have an impact on production. Phase space considerations can be used to estimate the suppression for associated

---

[1]The calculations assume positive parity for the Ξ_5 states, which is consistent with the chiral soliton model. Negative parity states would have smaller cross sections.
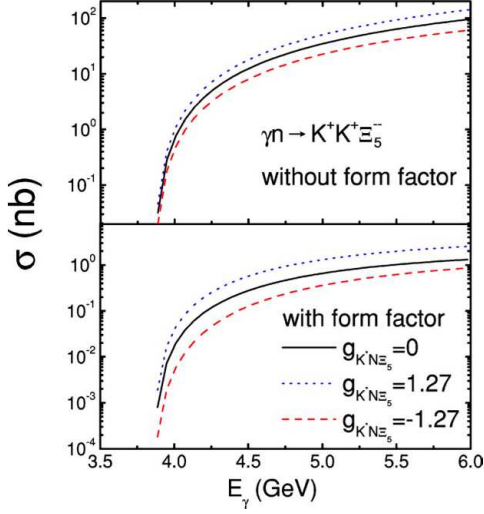
5

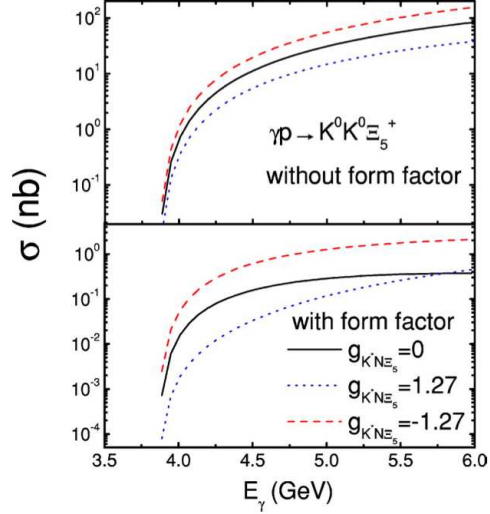Figure 2: Cross section for the production of $\gamma n \to K^+ K^+ \Xi^{--}$ from Ref. [22].

Figure 3: Cross section for the production of $\gamma p \to K^0 K^0 \Xi^+$ from Ref. [22].

pion production. We estimate that reactions with one additional pion will increase the threshold from 3.9 to 4.3 GeV and will result in a 30% reduction in the cross section.

1.3 Branching fraction

The present experiment will set limits on the product of cross section times branching fraction, so we describe some of the estimates for branching fractions simply as background for interpretation of the measurements. The most promising topology for our experiment results from the decay sequence $\Xi^{--} \to \pi^- \Xi^- \to \pi^-(\pi^- \Lambda) \to \pi^- \pi^-(\pi^- p)$. Within the diquark model [19, 24] and assuming $SU(3)_f$ flavor symmetry, the amplitude for $\Xi^{--} \to \pi^- \Xi^-$ is the same as $\Xi^{--} \to K^- \Sigma^-$. However, assuming P-wave phase space suggested by the diquark picture and the mass of the cascade pentaquark of about 1.86 GeV, the branching fraction $Br(\Xi^{--} \to \pi^- \Xi^-) \approx 0.67$. Modeling based on partial wave analysis of resonances gives a range of estimates for the ratio of $\Xi^{--} \to \pi^- \Xi^-$ to $\Xi^{--} \to K^- \Sigma^-$ ranges from 1.3 to 26 [25] depending on the anti-decuplet coupling constant. In summary, although there is a large range in the predictions, the cascade pentaquark decay mode to three pions

6

and one proton is expected to be dominant.

2 Experimental Data from CLAS

The eg3 data was collected in December of 2004 and January of 2005, dividing the run into two segments, which we will refer to as before Christmas and after Christmas, respectively. The detector configuration was chosen to satisfy the specification described in the experimental proposal [26]. The electron beam energy averaged from the reported by the Hall A and C arc measurements was 5765.5 MeV and 5768.3 MeV before and after Christmas, respectively. The electron beam passed through a radiator with a nominal thickness of 5×10^{-4} r.l. and was bent into the CLAS tagging system, where the electron energy was measured. The photon beam from the radiator impinged upon a 40 cm long and 4 cm diameter liquid deuterium target positioned 50 cm upstream of the nominal CLAS target position. The standard electron beam current was chosen to be 30 nA, and it was limited by the drift chamber performance. There were two Level 1 trigger configurations selected as trigger bits five and six. Trigger bit five was set as a two track trigger requiring a coincidence in the TOF system and start counter in the same sector in at least two sectors: $(TOF \times ST)^2$. Trigger bit six was a three track trigger requiring TOF and ST coincidences in at least three sectors : $(TOF \times ST)^3$. The bit 5 trigger was prescaled with a factor which varied from run to run to allow for less than 20% deadtime. The Level 1 trigger was in coincidence with the Master OR signal from the photon tagger. For a large portion of the run the Master OR also passed through a coincidence with the Start Counter before going into the trigger supervisor in order to reduce the trigger background rate. This experiment did not use the Level 2 trigger capability of CLAS.

3 Data Reduction and Processing

The raw data from the CLAS detector were recorded on the tapes of the Jefferson Lab tape silo in BOS format files [27]. After the calibration of all subsystems was finished, these files were retrieved from the silo and processed using the off-line event reconstruction code. For each raw data file a single job was launched on the Jefferson Lab Linux batch farm. For each job a raw data

file was analyzed and an output ("cooked") BOS file was produced. Then a sequence of filtering programs, selecting a significantly reduced data sample, were run on the output files to produce filtered BOS files, which contained the same BOS banks [27] but for far fewer number of events. These kinds of filtering (or skimming) procedures are effective for reactions with relatively small cross sections, such as processes involving production of strange particles. In addition, ROOT [28] files, containing ROOT trees, were produced from the cooked and filtered files. The ROOT files are relatively smaller in size than the BOS files, and they contain information from only the essential for analyses BOS banks. This makes them more convenient for a higher level analysis, involving a smaller subset of total events. The runs used in this analysis are given in Appendix A.1. The current analysis described in this paper was done using skimmed ROOT files containing at least one candidate for $\Lambda(1116)$.

4   Identification of $\Lambda(1116)$

The first step for the event selection chain for this analysis is identification of the $\Lambda(1116)$ charged decay products - a proton and a π^-. The files from Λ-skim are already preselected to contain only events with at least one Λ candidate pair, which is one positive and one negative time based tracks with invariant mass restrictions :

$$(|M_c - 1.1157 \texttt{ GeV}| < 0.017 \texttt{ GeV}) \oplus (|M_u - 1.1150 \texttt{ GeV}| < 0.017 \texttt{ GeV}), \quad (1)$$

where M_c and M_u are corrected and uncorrected for energy loss invariant masses of the pair. The invariant masses are calculated by assuming that the negative particle in a pair is a π^-, and the positive particle is a proton. The effects of the energy loss corrections are described in Section 6. No other cuts were used during filtering Λ-skim files.

In the offline analysis additional requirements are applied to select proton and π^- from Λ-decays. In this procedure we consider all possible pairings of negative and positive tracks, similar to what is done during skimming. But here the energy loss is already applied to the momentum of the both particles. For each pair we assume that the negative particle in a pair is a π^-, and the positive particle is a proton. First we require that the vertex times of the proton and π^- be within ± 2 ns from each other. For protons with higher momentum the timing cut is more narrow. The momentum of
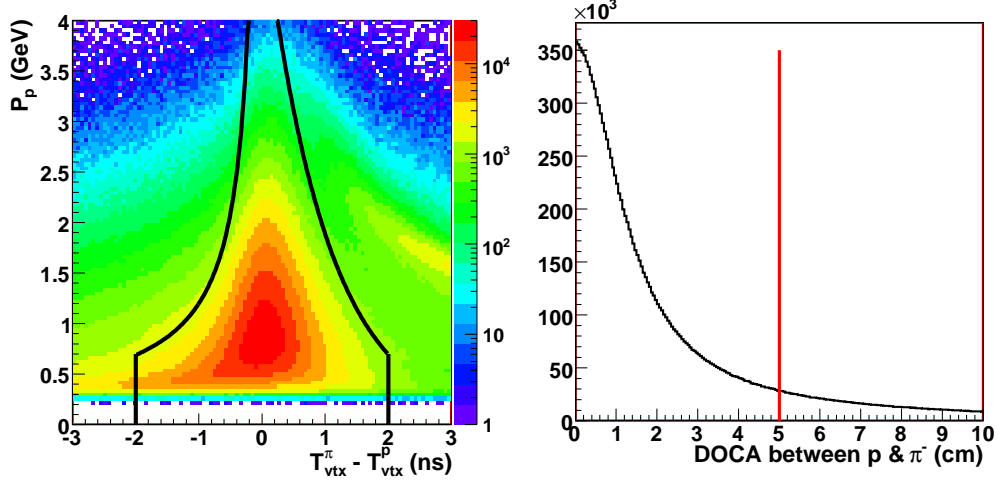
Figure 4: The momentum of the proton candidates versus the time difference between the proton and π^- (left). The black lines show the timing cut on the Λ-candidate pair. On the right panel is the DOCA distribution between proton and π^- tracks. The red line shows the maximum allowed vertex DOCA for the Λ-candidates in this analysis.

the proton candidate versus the vertex time difference between protons and negative pions is shown in Fig. 4 (left). All events between the black curves and $P_p = 0.150$ GeV were considered for further analysis.

Because the decay products originate from the same point in space, a 5 cm cut is applied on the Distance-Of-Closest-Approach (DOCA). DOCA is defined as the shortest line segment connecting straight lines defined by track momentum and vertex position information from the EVNT bank. DOCA distribution is shown in Fig. 4 b. The invariant mass cut applied in the offline analysis is 1.1120 GeV$< M_{p\pi^-} <$ 1.1206 GeV[2]. If there are more than one $p - \pi^-$ pairs satisfying this criteria the best pair is selected which yields the minimal value for quantity χ^2_Λ defined as:

$$\chi^2_\Lambda = \left(\frac{M_{p\pi^-} - M_\Lambda}{0.0017 \text{ GeV}}\right)^2 + \left(\frac{T_p - T_{\pi^-}}{0.45 \text{ ns}}\right)^2 + \left(\frac{DOCA(p\pi^-)}{1.5 \text{ cm}}\right)^2, \qquad (2)$$

where M_I is the invariant mass of the pair, T_p and T_{π^-} are vertex times of

___

[2]The cut is actually applied on the invariant mass of the pair after the energy loss and momentum corrections are applied.

9

proton and π^-.

5 Identification of negative pions

After we found the $\Lambda(1116)$ decay products using the procedure described in Section 4 we can assume with more certainty that the negative particle in the pair is a π^-, and use this hypothesis to verify the start time of the event. The standard SEB package does determine the event start time based on the vertex times of all the tracks in the event, also taking into account the offset of the event interaction with respect to the center of the target. The SEB procedure attempts to find the right RF bucket associated with the electron beam bunch by matching the tagger RF time with the vertex time reconstructed by the CLAS. Due to the large number of the hits in the tagger at the EG3 running condition this matching is not always correct. For that reason we use the vertex time of the π^- from the Λ-decay instead of a photon from the tagger hodoscope to reselect the RF bunch. Note that the RF signal does not have to be present in the data stream since the SEB start time is already determined from the photon time in the tagger, and the photon time in the tagger is very closely correlated with the RF bucket time within 200 ps.

We offset the start time of the event contained in the HEVT bank by a multiple of 2.004 ns required by the vertex time of the π^-. The vertex time is defined as the pion vertex time. This time is not propagated to the target center; instead, it is directly compared with the start time given in the HEVT bank, and the required time offset multiple of 2.004 ns is obtained:

$$T_0^{new} = T_0^{SEB} - 2.004 \text{ ns } R\left(\frac{T_0^{SEB} - T_{\pi^-}}{2.004 \text{ ns}}\right), \qquad (3)$$

where T_0^{new} is the new adjusted start time for the event, T_0^{SEB} is the original event start time from the HEVT bank, T_{π^-} is the vertex time of the negative pion, and the 2.004 ns is the bunch separation time for the Hall B electron beam. R stands for rounding up to the nearest integer number. A comparison of the velocity β of the negative tracks determined from the time-of-flight system of CLAS versus their momentum before and after adjustment of the event start time is shown in Fig. 5, panels a and b respectively. One can clearly see that the start time adjustment procedure significantly reduced the whisker-like structures due to RF bucket misidentification when a wrong
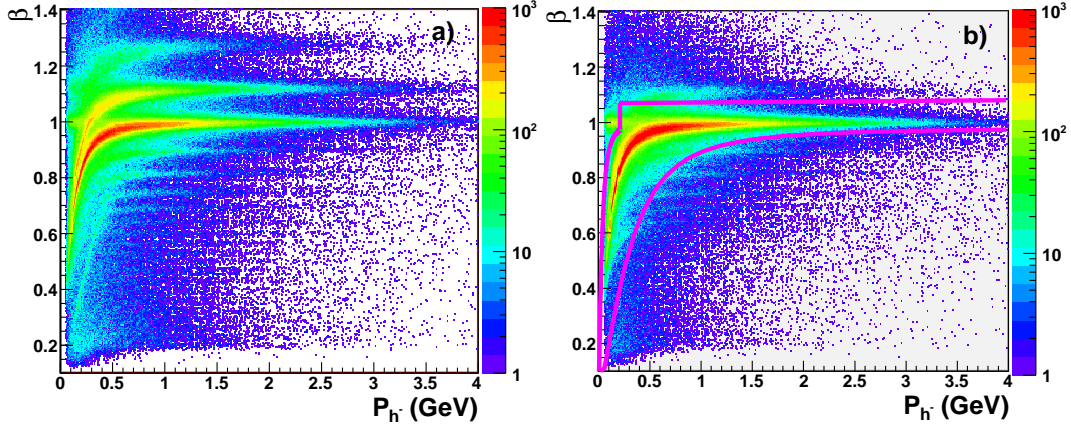
10

Figure 5: Plots of β from SEB (a) and β with adjusted start time (b) versus momentum of negative tracks from Λ skim files. The magenta curves in the right panel indicate the boundaries of the π^- selection area.

photon is selected in the tagger. Once the event start time is determined, the negative pions are identified by comparing imposing cuts on the β versus momentum plot as illustrated by magenta curves in Fig. 5 b.

6 Energy Loss Correction

When particles from the photon-target interaction pass through the material in the target region of CLAS they may lose part of the energy due to ionization. The amount of the energy loss depends on the charge and the velocity of the particle, and the type and amount of the material it traverses. In order to account for these effects energy loss corrections were applied according to *eloss* procedure [29]. A comparison of the $\Lambda(1116)$ mass before and after energy loss corrections is shown in Fig. 6. The peak becomes more narrow $\sigma_\Lambda \sim 1.5$ MeV, and the location of the peak becomes more consistent with the PDG value of $M_\Lambda = 1.115683$ GeV. Most of the improvement comes from the corrections for the negative pions from $\Lambda(1116)$ decays that have energy typically less than 500 MeV. The average mass resolution of the $p\pi^-$ system in this data sample is about 1.6 MeV. The energy loss corrections are applied to all particles involved in this analysis.
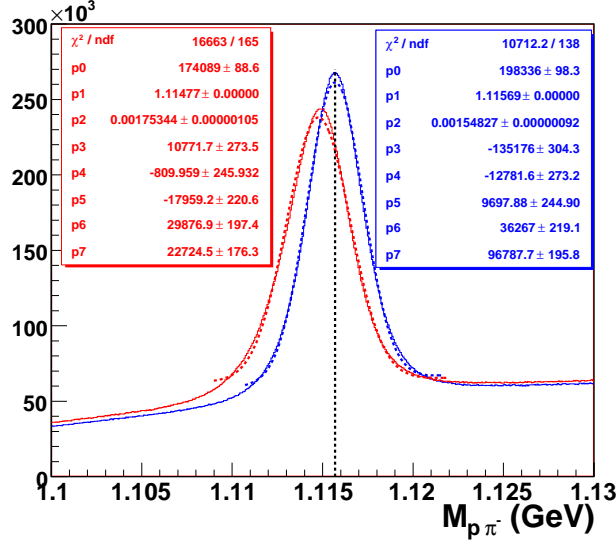
11

Figure 6: Mass spectrum of the $p\pi^-$ system before (red) and after (blue) energy loss corrections are applied. The dashed vertical line shows the PDG [2] value for the mass of $\Lambda(1116)$.

7 Momentum Corrections

Even after energy loss corrections are performed, systematic errors still remain in the particle momentum determined from CLAS using the standard reconstruction software. These errors can be due to the misalignment of the torus magnet cryostats with respect to the CLAS drift chambers, energy loss of particles in the drift chamber region not accounted for in the *eloss* package [29], or software or calibration shortcomings. These errors in the momentum determination can lead to shifts of the masses of decayed or missing particles and widening of the peaks.

To correct the track momentum, the $\gamma D \to pp\pi^-$ reaction was kinematic fit requiring four-momentum conservation [30]. The proton and π^- track momentum were treated as unknown to remove their bias from the fit. The momentum corrections for protons and π^-'s were fit separately as they bend in different directions in the magnetic field. Since $\frac{\int Bdl}{p}$ is the quantity that is measured, the difference between the fit and measured track momentum was fit as a function of $\delta(1/p)$ to correct for errors in measurement.

The average difference between fit and measured momentum was up to 15

12

MeV when studied versus track ϕ, most likely due to errors in the magnetic field map and drift chamber misalignments. These were corrected by fitting $\delta(1/p)$ linearly in 1/p in 5 degree bins of ϕ.

For protons, the average difference between fit and measured momentum was up to 10 MeV for low momentum tracks. This was most likely due to energy losses in the drift chambers, and was corrected by fitting the energy loss as a decaying exponential.

Finally, the θ dependent drift chamber misalignments were studied as a function of θ. These were found to only be about 5 MeV, and were corrected by fitting $\delta(1/p)$ as a 7th order polynomial function of θ.

The resulting momentum corrections were small, and their application does not change the main conclusions of this analysis.

8   Selection of $\Xi^-(1321)$ events

After selecting the best candidate pair for $\Lambda(1116)$ we proceed with combining it with the remaining negative pions in the event. For further analysis we require that an event contained at least two more negative pions in addition to the π^- in the $\Lambda(1116)$-pair. Therefore one can have multiple combinations of pairings ($\Lambda\pi^-$). One either can use all combinations, or, alternatively, one could select the pair which is most consistent with a ground state cascade $\Xi(1321)$ based on the vertex information and the invariant mass. The former yields worse signal-to-background ratio, while the latter, although provides better signal-to-background ratio, can distort the content of the sidebands around the cascade peak. We tried both approaches in our analysis, and they are described in the subsection below.

8.1   Liberal Selection of Events

First we attempt to obtain an event ensemble which provides a very good signal-to-background ratio with little concern about quality of the events. This means that we neither select the best runs, nor do we apply fiducial cuts or matching between a photon in the tagger and the event detected in CLAS. With this kind of selection of events we merely try to see if we can see any enhancement in the $\Lambda(1116)\pi^-\pi^-$ invariant mass. For each event we only select one $\pi^-\Lambda$ pair for which the common vertex and the invariant mass are most consistent with a decaying ground cascade. The selection criteria
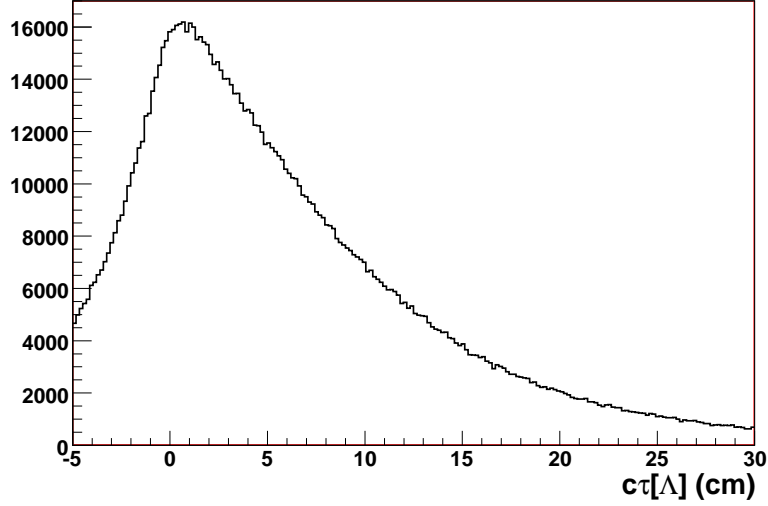
13

Figure 7: Typical distribution of $\widetilde{c\tau}$ for $p\pi^-$ system assuming it is a $\Lambda(1116)$. The Λ-production vertex is defined by the intersection point of the Λ-candidate and another π^-.

is to minimize the following quantity:

$$\chi_\Xi^2 = \left(\frac{M_{\Lambda\pi^-} - M_\Xi}{2.1 \text{ MeV}}\right)^2 + \left(\frac{DOCA(\Lambda\pi^-)}{2.25 \text{ cm}}\right)^2 \qquad (4)$$

We also improve the Λ selection by applying a cut on $c\tau$ of the Λ-candidate. In this analysis we define a signed version of the $c\tau$ quantity as the projection of the measured $c\tau$ onto the the the axis along the momentum of $P\pi^-$ combined system:

$$\widetilde{c\tau} = \frac{\Delta\vec{V_\Lambda} \cdot \vec{P_\Lambda}}{|P_\Lambda|}\sqrt{\frac{1}{\beta_\Lambda^2} - 1} \qquad (5)$$

Figure 7 shows a typical $\widetilde{c\tau}$ distribution for Λ-candidates. The shape of the distribution is consistent with convolution of a exponential function and a Gaussian. The position of the peak is mostly determined by the resolution of the detector, and the slope of the function away from 0 is primarily determine by the decay constant $c\tau$.

A similar cut quantity can also be defined for decaying $\Xi^-(1321)$, where the upstream vertex of Ξ-production is defined by intersection of the tracks
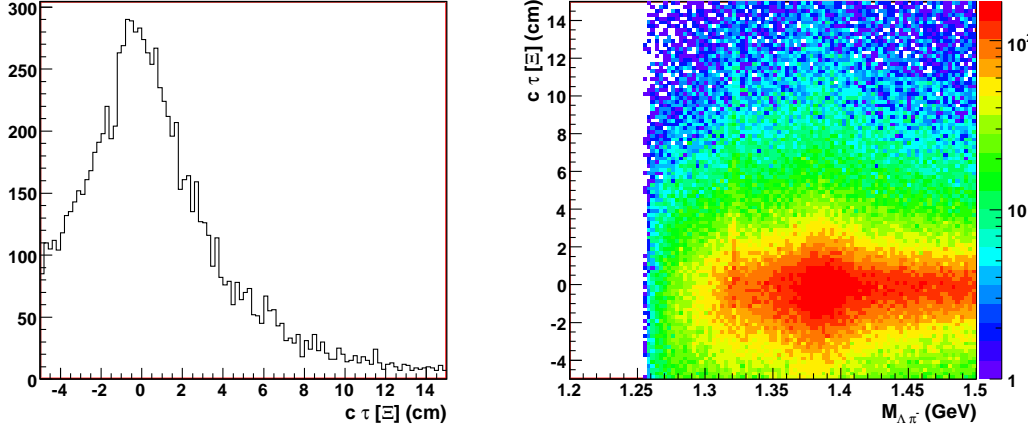
14

Figure 8: Distribution of $\widetilde{c\tau}$ of $\Lambda\pi^-$ system with "liberal selection" assuming it is a $\Xi^-(1321)$ (left). Distribution of $\widetilde{c\tau}$ versus invariant mass of $\Lambda\pi^-$ system with "liberal selection" before applying the invariant mass cut (right). The vertical band corresponding to $\Xi^-(1321)$ extends to larger values of $\widetilde{c\tau}$ providing an extra handle for selecting desired events.

from the Λ and the next π^-. A two dimensional plot showing the proper time $\widetilde{c\tau}$ of the assumed $\Xi^-(1321)$ versus the invariant mass of $\Lambda\pi^-$ system is shown on Fig. 8. The proper time $\widetilde{c\tau}$ for $\Xi^-(1321)$ is defined similar to Eq. 5, but exchanging $\Lambda(1116)$ for $\Xi^-(1321)$. The cascade ground $\Xi(1321)$ weakly decays into $\Lambda\pi$, and has a width negligible compared to the CLAS energy resolution, while the $\Sigma^-(1385)$ decays into $\Lambda\pi$ through strong interaction with a relatively large width of 39.4 MeV [2], creating background to $\Xi(1321)$ events. A vertical band corresponding to $\Xi^-(1321)$ extends to quite large values of $\widetilde{c\tau}$, therefore providing an additional handle for enhancing the signal-to-background ratio. After applying a cut $\widetilde{c\tau} > 1.5$ cm we get a relatively clean $\Xi^-(1321)$ peak containing ~ 1700 events with signal-to-background ratio of ~ 0.8 (see Fig. 9 a).

In fact we can even improve the signal-to-background ratio by requiring an additional K^+ in the event. This reduces the number of events by a factor of two. The invariant mass of $\Lambda(1116)\pi^-$ system with an additional kaon is shown in Fig. 9 b.
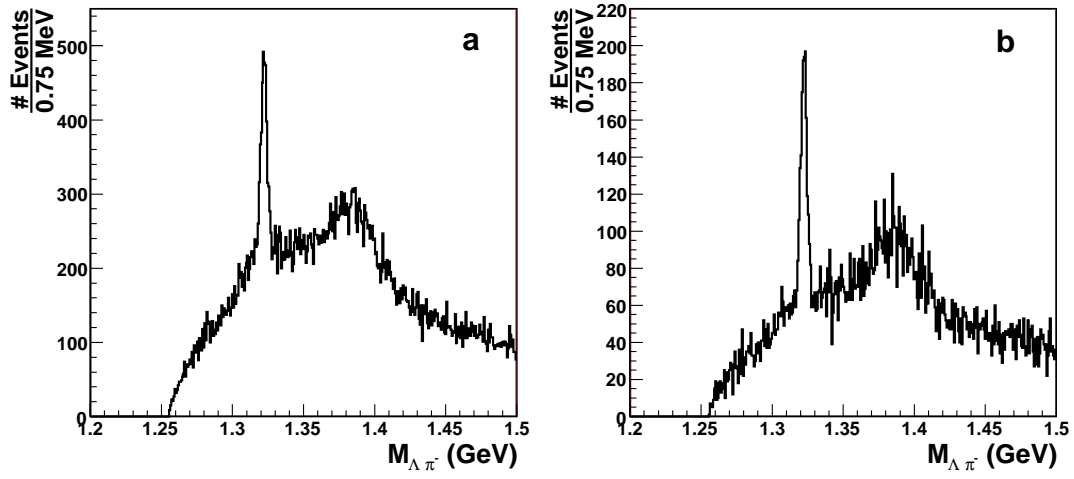
15

Figure 9: Invariant mass distribution of $\Lambda\pi^-$ system with "liberal selection" with an extra lifetime cut $\widetilde{c\tau} > 1.5$ cm for $\Lambda\pi^-\pi^-$ events (a) and $K^+\Lambda\pi^-\pi^-$ events (b).

Cut ID	Cut Values
$\Delta T(\Lambda)$	See Fig. 4 (left)
DOCA(Λ)	DOCA(Λ) ≤ 5.0 cm
Mass(Λ)	1.1108 GeV $\leq M_\Lambda \leq$ 1.1202 GeV
$c\tau(\Lambda)$	1.5 cm $\leq c\tau(\Lambda) \leq$ 25 cm
DOCA(Ξ)	DOCA(Ξ) ≤ 4.5 cm
Mass(Ξ)	1.3175 GeV $\leq M_\Xi \leq$ 1.3265 GeV
$c\tau(\Xi)$	1.5 cm $\leq c\tau(\Lambda) \leq$ 25 cm
DOCA($\Xi\pi$)	DOCA($\Xi\pi$) ≤ 4.5 cm

Table 2: Summary of all cuts for the "liberal selection" of events.

16

8.2 Conservative Selection of Events

To obtain absolute cross sections or their upper limits with CLAS we need to select only events from the runs which did not have significant hardware problems, use only tracks in the fiducial regions of CLAS, and also be able to match the event with one of the tagger E-counters. In our case the possible photon range should be within the tagger Master OR (MOR) range used in coincidence with Level 1 trigger. In addition, if one would like to extract the number of the events containing $\Xi^-(1321)$ using sideband subtraction or fitting, then selecting only the "best" $\Lambda\pi^-$ will distort the shape of the background resulting in a more ragged structure underneath and around the $\Xi^-(1321)$ mass peak. Therefore, all combinations of the Λ and each of the remaining pions in the event are considered, and are included in the invariant mass spectrum of $\Lambda\pi^-$ system. Note that such a treatment of the $\Lambda\pi^-$ pairs double- or triple-counts the background, but it only counts the cascade event once. The cuts used in this selection are slightly different than what is used in Sec. 8.1, and are given in Table 3. The detached vertex cuts on $\widetilde{c\tau}$ were removed because of the difficulty associated with the reproduction of the vertex distribution in the simulations.

The invariant mass distribution of the $\Lambda\pi^-$ pairs shown in Fig. 12 features two very distinct structures: first is a narrow structure near $M = 1.321$ GeV corresponding to $\Xi(1321)$, and the second one is a broader structure center at $M = 1.385$ GeV corresponding to $\Sigma^-(1385)$. This selection does not distort the backround, and we can apply the sideband subtraction method to obtain the $\Xi(1321)\pi^-$ mass spectrum. But these selection of events drastically reduces the number of events in the cascade peak. The number of events in the $\Xi^-(1321)$-peak is given in the Table 4. Although the signal-to-background ratio improves with tightening the $\widetilde{c\tau}$ cut, the number of event in the peak reduces. Our studies could not confirm that this reduction in events is well reproducible in GSIM. Therefore, in the following sections we will be using only $\widetilde{c\tau} > -25$ cm cut, which is almost equivalent of having no cut at all.

9 Fiducial and Energy Cuts

There were two additional kinds of cuts in this analysis applied to both the real data and the Monte Carlo (MC) simulations. The first kind are the geometrical fiducial cuts, applied in order to select the regions of the

17

Cut ID	Cut Values
$\Delta\mathrm{T}(\Lambda)$	See Fig. 4 (left)
DOCA(Λ)	DOCA(Λ) $\leq$ 5.0 cm
Mass(Λ)	1.1108 GeV $\leq M_\Lambda \leq$ 1.1202 GeV
DOCA(Ξ)	DOCA(Ξ) $\leq$ 4.5 cm
Mass(Ξ)	1.3175 GeV $\leq M_\Xi \leq$ 1.3265 GeV
DOCA($\Xi\pi$)	DOCA($\Xi\pi$) $\leq$ 4.5 cm

Table 3: Summary of all cuts for the "conservative selection" of events.

relatively uniform detector response which could also could be reproduced by the *GSIM* simulation program. These cuts select angular ranges in the laboratory frame for various values of 3-momentum of positive and negative particles. Sample plots of these cuts for π^- are shown in Fig. 10, and for protons are shown in Fig. 11. The blue areas are the accepted events, the red areas are rejected events.

The second kind are the kinematic cuts which can be imposed on the kinematic quantities to enhance the signal. In this analysis we can impose such a cut on the missing mass of the remaining system after $\Xi(1321)^-\pi^-$ system is identified. To conserve strangeness in the strong and electromagnetic interactions leading to cascade photoproduction we can expect two addition kaons to be produced on deuteron. This can be utilized by requiring at least one tagger hit matching in time and satisfying the missing mass contraint:

$$M_{miss} = \sqrt{[(p_\gamma + p_d) - (p_{\Xi^-} + p_{\pi^-})]^2} > 2M_{K^+} + M_n, \qquad (6)$$

where p_γ, p_d, p_{Ξ^-}, and p_{π^-} are 4-vectors for the photon, deuteron, $\Xi(1321)^-$, and π^- respectively. Only tagger hits with status word in the TAGR bank equal to 7 or 15 were used, and the timing window to match the CLAS event start time and the tagger hit time was 0.8 ns. In addition only tagger E-counters from 1 to 175 were used because they match the T-counters from 1 to 19 which were included in the tagger part of the trigger. Note that tagger cut is only imposed when cross section is calculated. This cut is not present in the cases of "Liberal Selection" of events described above in Sec 8.1.
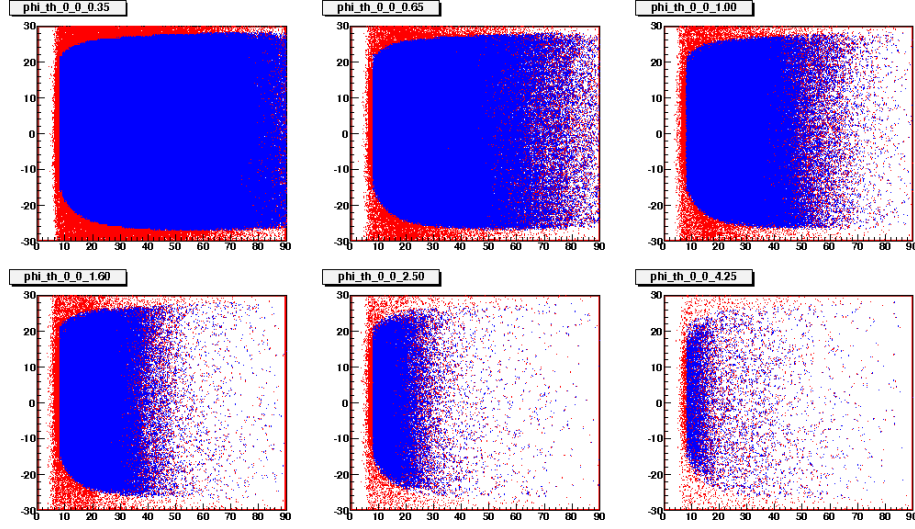
Figure 10: Laboratory angles ϕ versus θ for negative tracks in Sector 1 for various momentum ranges. The red areas are rejected regions, the blue areas are the accepted regions.

Figure 11: Laboratory angles ϕ versus θ for positive tracks in Sector 1 for various momentum ranges. The red areas are rejected regions, the blue areas are the accepted regions.

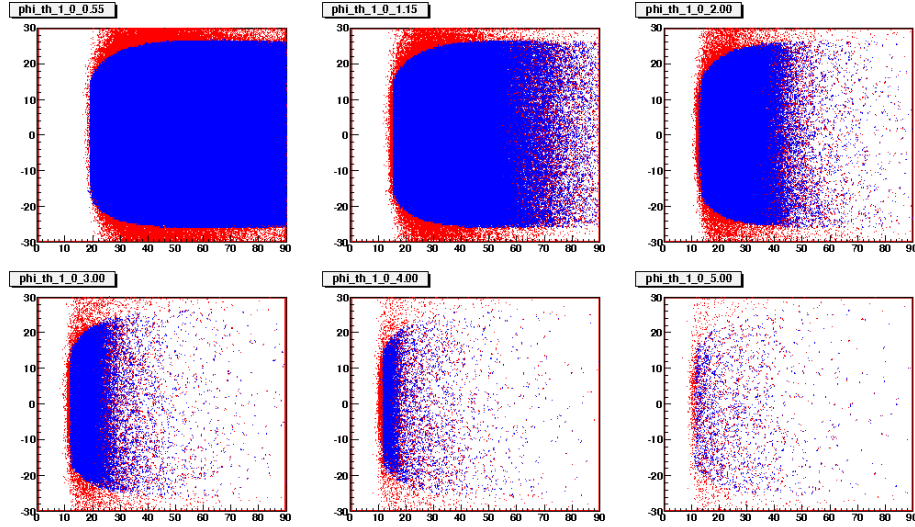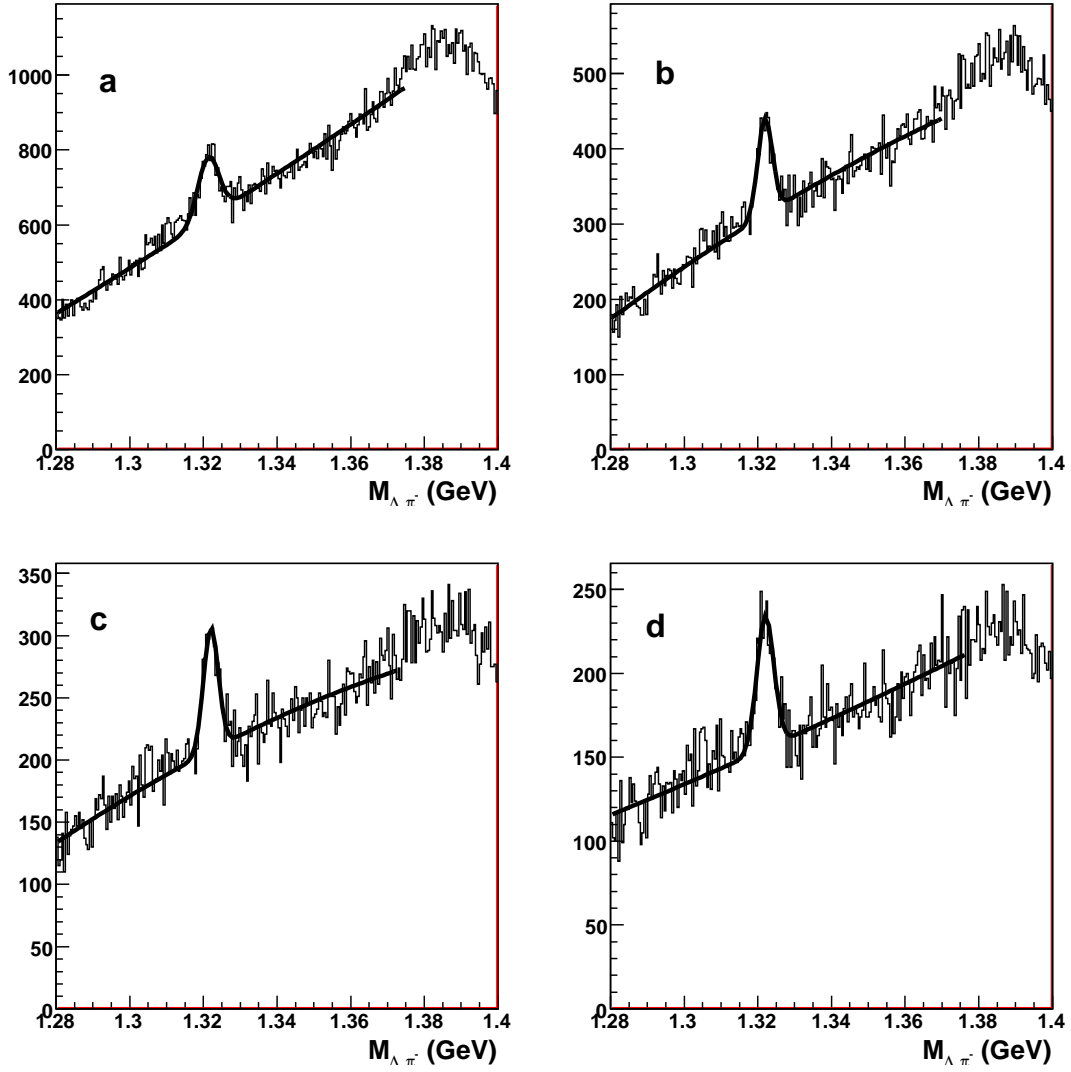Figure 12: Invariant mass distribution of $\Lambda\pi^-$ system with "conservative selection" with four different $\widetilde{c\tau}$ cuts for $\Lambda\pi^-\pi^-$ events: a) $\widetilde{c\tau} > -25$ cm; b) $\widetilde{c\tau} > 0$ cm; c) $\widetilde{c\tau} > 1.5$ cm; d) $\widetilde{c\tau} > 2.5$ cm. The fiducial cuts are applied as well.

20

Cut on $\widetilde{c\tau}$	Number of Ξ^-s	Sig/Bkg Ratio
$\widetilde{c\tau} > -25$ cm	2004	0.19
$\widetilde{c\tau} > 0$ cm	1228	0.23
$\widetilde{c\tau} > 1.5$ cm	956	0.28
$\widetilde{c\tau} > 2.5$ cm	852	0.33

Table 4: Number of events and the signal-to-background ratios for different $\widetilde{c\tau}$ cuts in Fig. 12.

10   Acceptance

10.1   Definition

In order to relate the experimental yields to the cross sections, one needs to calculate the acceptance and the efficiency of the detector. Since CLAS is a very complicated detector covering almost 4π of solid angle, it is virtually impossible to separate efficiency calculations from geometrical acceptance calculations. For this reason in this analysis we refer to acceptance corrections as a combined correction factor due to the geometry of the detector and the inefficiencies of detection and reconstruction. Our definition of acceptance is the ratio of the number of reconstructed simulated events in a invariant mass bin to the total number of simulated events for the same bin. Since the detector has a finite resolution it is possible that an event produced in one bin is reconstructed in a different bin, and therefore one would need a matrix to fully account for such bin migration effects. If the number of events created in the i-th bin is N_i and the number of reconstructed events in j-th bin is R_j, then:

$$R_i = \sum_j M_{ij} N_j, \qquad (7)$$

$$N_i = \sum_j M_{ij}^{-1} R_j, \qquad (8)$$

where M_{ij} is a large $N_{bin} \times N_{bin}$ square matrix. But in order to be able to use such a method one would also need a very large number of simulated events, which is not affordable due to the slow (1.5 event/sec) speed of the detector simulation program. In addition, the determination of the inverse of such a large square matrix is known to be a very unstable procedure.

21

But if the event generator produces realistic distributions, then one does not need the full matrix and our definition of the acceptance as a ratio would suffice. However, the remaining model-dependence of the final results should be estimated as systematic uncertainty (see Sec. 12). The tagger inefficiency is cancelled out in the normalization procedure, therefore the tagger responce is not included in the acceptance and efficiency calculations.

The acceptance corrections were applied on a bin-by-bin basis. Each bin was weighed by a factor determined from an acceptance one-dimensional histogram. This factor is defined as the ratio of number of events reconstructed in a given bin to the number of generated events:

$$A = \frac{N_{rec}}{N_{gen}}. \tag{9}$$

In this case the uncertainty of the cross section is due to statistics in the data sample and the uncertainty in the acceptance:

$$\left(\frac{\delta\sigma}{\sigma}\right)^2 = \frac{1}{N} + \frac{\delta A^2}{A^2}, \tag{10}$$

where N is the number of events in the data bin, A and δA are the acceptance and the acceptance error for that bin. In this analysis the statistical error for the acceptance δA is determined using the formula for the binomial distribution:

$$\delta A = \sqrt{\frac{A(1-A)}{N_{gen}-1}}, \tag{11}$$

where N_{gen} is the number of the Monte-Carlo (MC) events generated in an acceptance bin.

10.2 Simulations

In order to calculate the acceptance, approximately 30 million $\gamma d \rightarrow K^+K^+\Xi^-\pi^- p_s$ events were generated using a phase space event generator [31] which also has the Fermi-motion smearing incorporated in it. The output file, containing "MCTK" and "MCVX" banks from the event generator, were fed to *GSIM* [32] - a program which simulates the response of the CLAS detector. The Čerenkov counter and tagger response from GSIM were not used. The former was not yet been adequately modeled and is not used in this analysis at

Cut ID	Cut Values
ΔT(Λ)	See Fig. 4 (left)
DOCA(Λ)	DOCA(Λ) $\leq$ 5.0 cm
Mass(Λ)	1.1108 GeV $\leq M_\Lambda \leq$ 1.1202 GeV
DOCA(Ξ)	DOCA(Ξ) $\leq$ 4.5 cm
Mass(Ξ)	1.3166 GeV $\leq M_\Xi \leq$ 1.3256 GeV
DOCA($\Xi\pi$)	DOCA($\Xi\pi$) $\leq$ 4.5 cm

Table 5: Summary of the cuts imposed on the simulated events.

all. The tagger efficiency is taken into account in the photon determination procedure. The GSIM geometry was set using the standard values from the straight track analysis [33] for the drift chambers and the survey geometry for the TOF system [34] by using the *GSIM* key "RUNG=10". In order to eliminate signals from known dead channels, the GSIM Post Processor (GPP) program was used to remove signals from dead wires in the drift chambers and bad tubes in the scintillator counters. It also allows the user to smear the distance-of-closest-approach distribution in the DC and the TOF signals to match the invariant mass distributions and timing spectrum in the real data. Then the *GSIM* files were processed with the RECSIS program to reconstruct the simulated events. The executable of the reconstruction program was build with the same *Pass2v1* set of libraries which were used for processing the actual data from the EG3 running period. In the final stage the output files were analyzed to produce the acceptance histogram. The same cuts used on the experimental data were also applied to the simulated data to determine the acceptance.

Figures 13 and 14 show the kinematic coverage of the particles in the simulations compared to the real data. The left columns are histograms from the data, and the right column are from the GSIM simulations using $K^+K^+\Xi^-\pi^-$ phase space. The first raw are the distributions for the reconstructed Λ, the second row is for reconstructed proton, and the last row are reconstructed π^-s. The event selection in the actual data included the cut on the invariant mass of $\Lambda\pi^-$ system to be consistent with $\Xi(1321)$ mass, and is given in the Table 3. Note that, although all events in the simulation originally contained a Ξ^- particle, the same mass cut was applied to them as well.
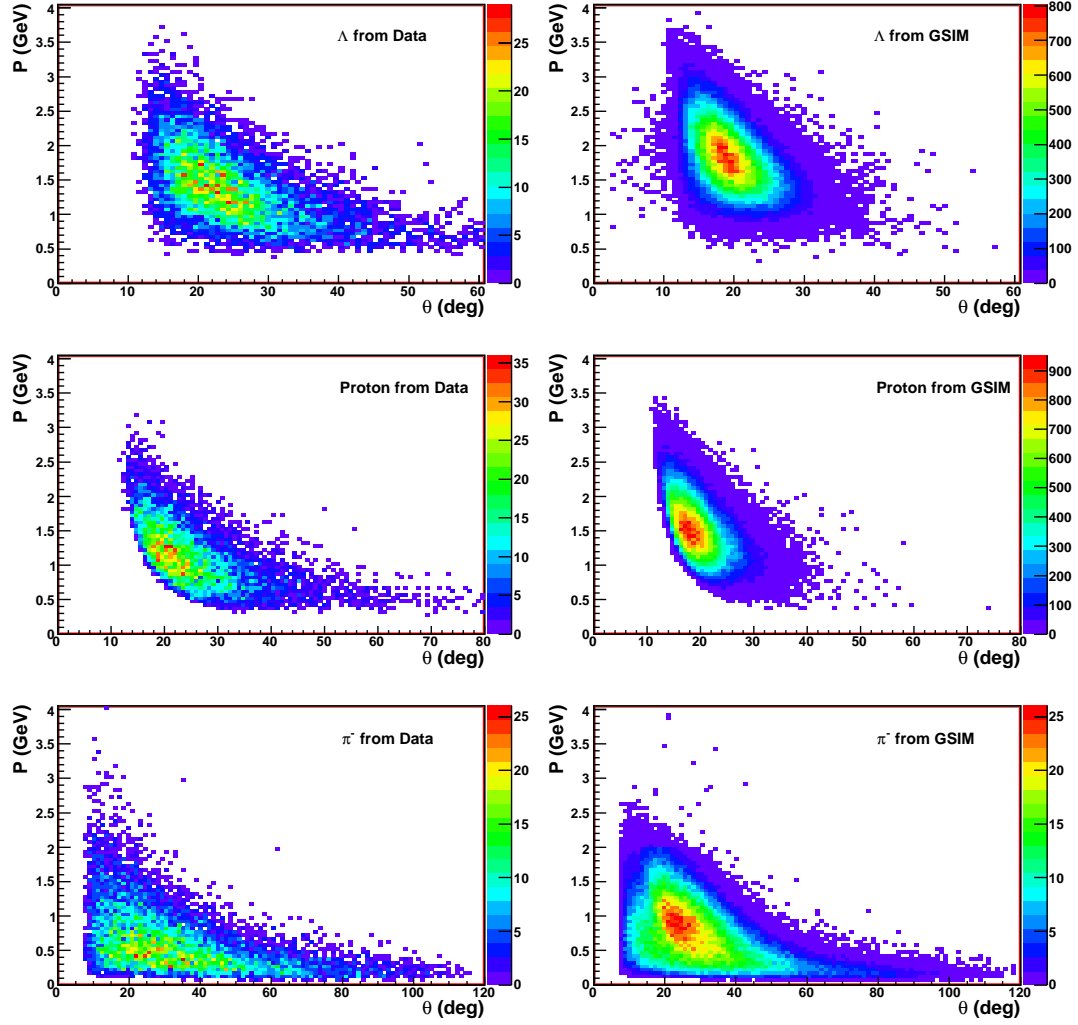
23

Figure 13: Momentum versus laboratory θ-angle distributions for the reconstructed particles. See text for explanations.
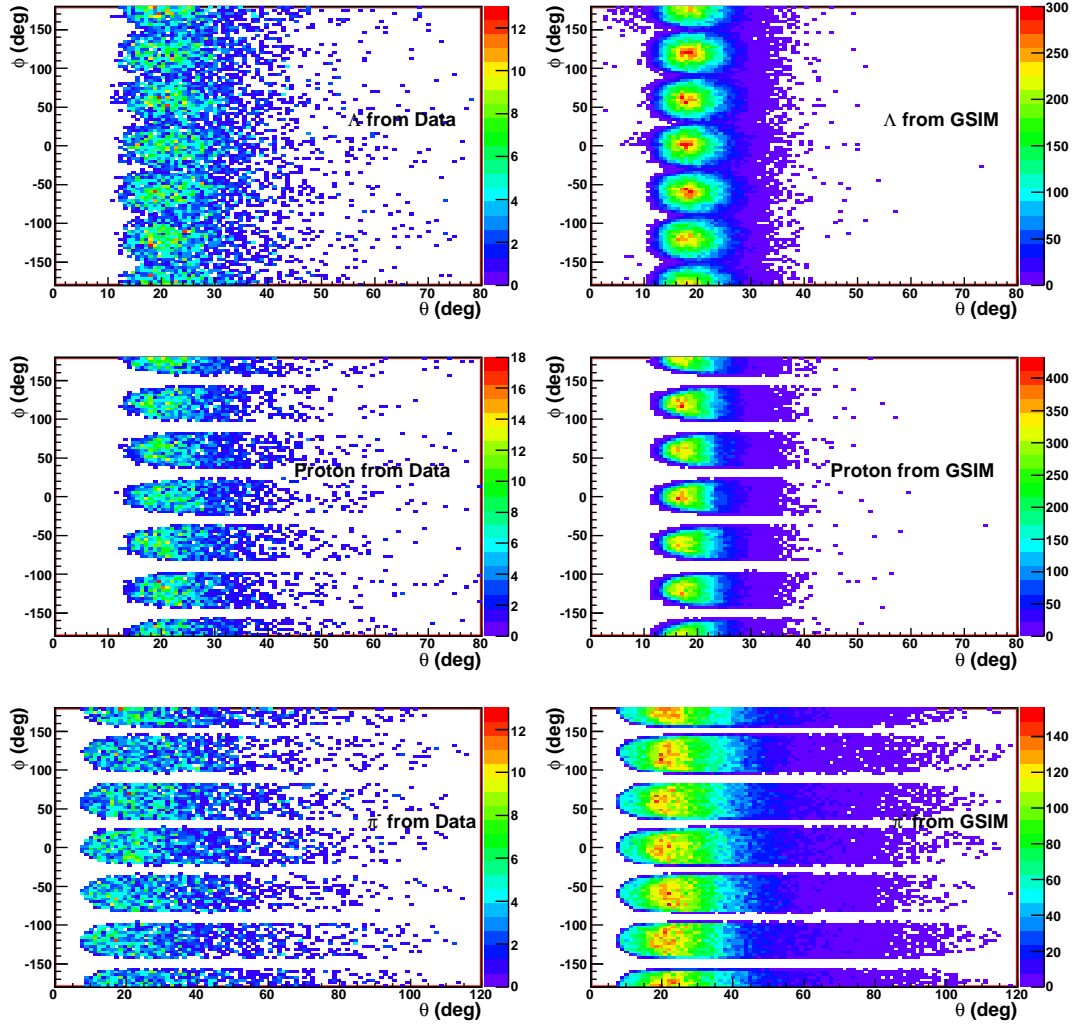
Figure 14: Azimuthal angle ϕ versus polar angle θ distributions for the reconstructed particles. See text for explanations.
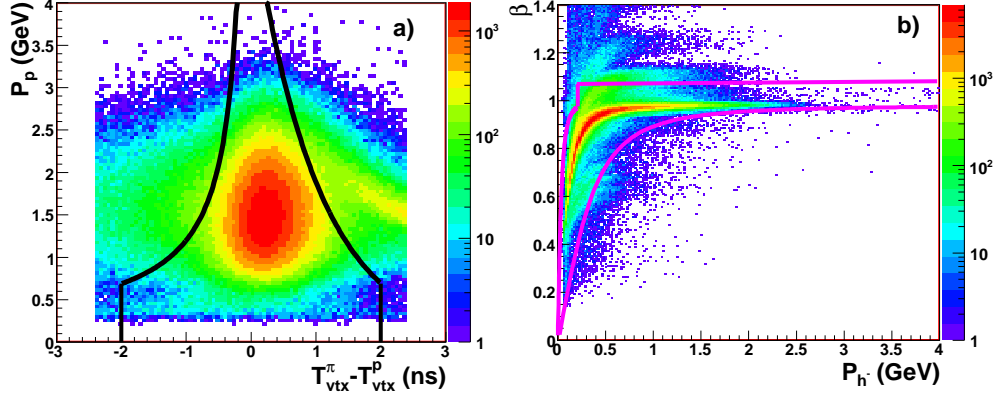
25

Figure 15: The momentum of the proton candidates versus the time difference between the proton and π^- (left). The black lines show the timing cut on the Λ-candidate pair. The right panel shows the π^- identification cuts applied on the remaining negative tracks in CLAS. The events in these plots are from GSIM.

The same cuts applied in the data were applied to the simulated events, and are given in Table 5. The small differences in the widths and the peak positions were taken into account by shifting and widening/narrowing the cuts in the appropriate directions, and are given in Table 5. Black curves in Fig. 15 a show the time difference cuts on the proton and pion candidates for selecting $\Lambda(1116)$ decay products, and the magenta curves Fig. 15 b show the remaining π^- identification cuts, applied on the simulated data sample.

The invariant mass spectrum for the $p\pi^-$, $\Lambda\pi^-$ and $\Xi^-\pi^-$ spectra from GSIM are shown in Fig. 16. The $p\pi^-$ spectrum features a peak due to $\Lambda(1116)$ which was in every simulated event. The $\Lambda\pi^-$ spectrum shows an enhancement near $M = 1.321$ GeV corresponding to the simulated $\Xi^-(1321)$. The $\Xi^-\pi^-$ spectrum shown here was produced with events which contained an infinitely narrow $\Phi^{--}(1862)$ state decaying into $\Xi^-\pi^-$, and the corresponding peak can be seen in Fig. 16 c. One also should note that the widths of these distributions are compatible with the data: the widths for $\Lambda(1116)$ in the simulations and the real data are $\sigma \sim 1.5$ MeV while the GSIM/GPP width for the $\Xi^-(1321)$ is ~ 2.2 MeV versus ~ 2.1 MeV in the data sample with the "conservative selection". The expected detector resolution for the $\Phi^{--}(1860)$ mass is ~ 7 MeV with a zero-width assumption in the event generator.
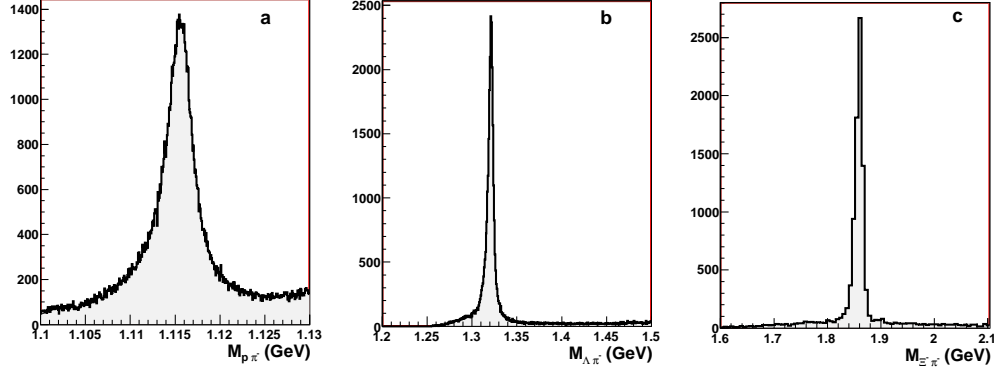
Figure 16: Invariant mass distributions from GSIM for $p\pi^-$ (a), $\Lambda\pi^-$ (b) and $\Xi^-\pi^-$ (c) systems. For all three cases the width of the distribution is due to the detector resolution.

ID	Simulated Reaction	$\frac{\delta A}{A}$
1	$\gamma d \to K^+ K^+ \Xi^- \pi^- p_s$	0 %
2	$\gamma d \to K^+ \Sigma^-(2650)p_s \to K^+ K^+ \Phi^{--}p_s \to K^+ K^+ \Xi^- \pi^- p_s$	+24 %
2	$\gamma d \to K_f^+ \Sigma^-(2650)p_s \to K_f^+ K^+ \Phi^{--}p_s \to K_f^+ K^+ \Xi^- \pi^- p_s$	+47 %
3	$\gamma d \to K^+ K^+ \Phi^{--}p_s \to K^+ K^+ \Xi^- \pi^- p_s$	+7 %

Table 6: Event configurations used for model dependence studies.

The CLAS acceptance versus invariant mass of $\Xi^-\pi^-$ system is shown in Fig. 17. The acceptance is small near the threshold, slowly increasing with the invariant mass. The value of the acceptance at mass $M_{\Xi^-\pi^-} = 1.860$ GeV is $\sim 0.3\%$.

10.3 Model Dependence

Because we do not know how the cross section of the $\Phi^{--}(1862)$ photoproduction depends on the kinematics, and we integrate over all of the kinematic variables, our estimate of the CLAS acceptance may also depend on the choice of the distribution of the events over phase space. In order to estimate the uncertainty of the acceptance due to the model dependence we performed a study using various distribution in the event generator. The studied configurations and the results are given in Table 6. The events were simulated
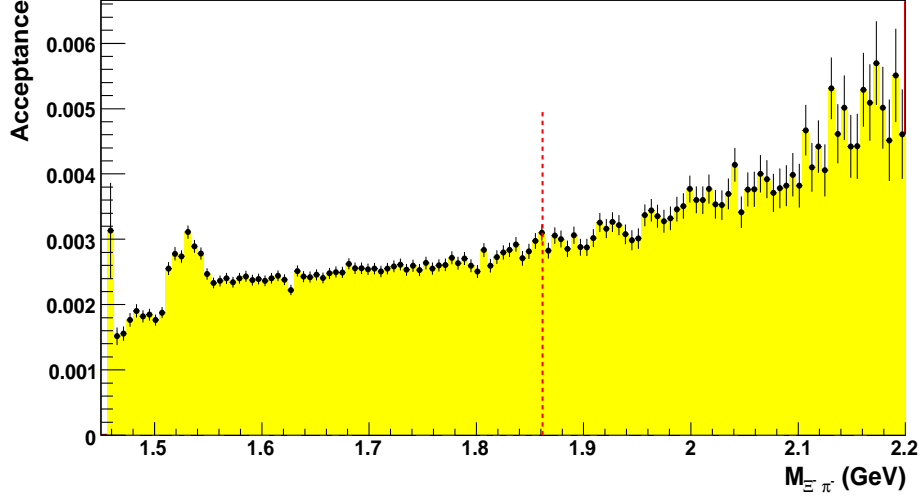
27

Figure 17: Acceptance of CLAS versus invariant mass of $\Xi^-\pi^-$ system determined from $\gamma d \to K^+K^+\Xi^-\pi^-p_s$ phase space simulation using GEANT-based detector simulation package GSIM. The red arrow points to the position of the peak seen by NA49 collaboration.

using *fsgen* package for simulating events according to flat phase space. The reaction # 1 in Table 6 is a four-body phase-space uniform distribution complemented with a spectator proton with a Fermi momentum smearing. For the process in row #2 a hypothetical $\Sigma(2650)$ was implemented in the code, that decayed into $K^+\Phi^{--}$ with total width of 35 MeV. The $\Phi^{--}(1862)$ was simulated as a particle with a infinitely narrow mass $M_\Phi = 1.862$ GeV decaying only through $\Xi^-\pi^-$ channel. The reactions #2 and #4 are simulated according to two- and three-body phase space accordingly, with a spectator proton with Fermi momentum. The process in row #3 in Table 6 is simulated according to two-body phase-space but with additional t-slope distribution for the K^+, taken with $b = 2.6$ GeV^{-2} t-slope paramater. Thus, the flat phase space is supposed to give us the estimate of the acceptance for the s-channel processes, while including a steep t-dependence would allow us to consider the processes going through the t-channel exchanges. Figure 18 shows the momentum-angle correlations of the accepted events from GSIM for the three described configuration of the event generator.

The third column is the deviation in percents from the acceptance value estimated with our standard channel with $\gamma d \to K^+K^+\Xi^-\pi^-p_s$ channel. For

28

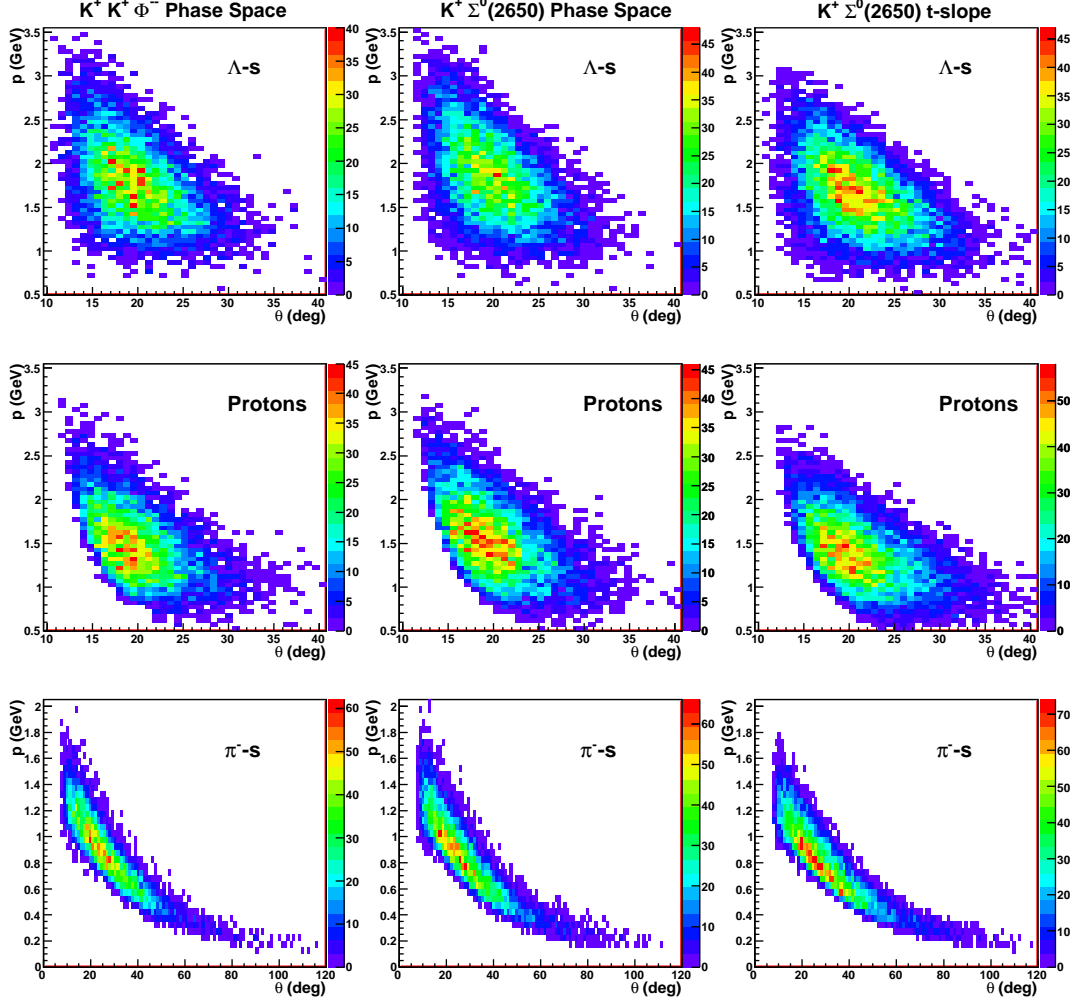Figure 18: Momentum versus laboratory angle θ for the Λs, protons and π^-s for reconstructed events from GSIM with the three event generator configurations from Table 6.

processes in rows from #2 to #3 the acceptance is estimated at a fixed mass $M_{\Xi^-\pi^-} = 1.862$ GeV since the process explicitly includes the $\Phi^{--}(1862)$ decay. For the case of the four-body phase space in raw #1 the acceptance is also estimated near $M_{\Xi^-\pi^-} = 1.862$ GeV. Because of these differences the code for acceptance estimation needs to be different for simulations with fixed and variable $M_{\Xi^-\pi^-}$ masses. In both cases the mass window is taken $\Delta M = \pm 10$ GeV to match the 20 MeV window for the upper limit estimation procedure. From this table we assign a relative uncertainty of $\frac{\sigma_A^{sys}}{A} \sim 20\%$ due to model dependence. This is one of the largest sources of uncertainty in the determination of the cross sections or its upper limits.

11   Normalization

In order to extract the absolute cross sections or the upper limit for the cross section one needs to determine the intergated luminosity corresponding to the analyzed data sample. The integrated luminosity per photon energy bin is given by

$$L = \frac{N_\gamma(E_{bin})\,\rho_D\,L_T\,N_A}{A_D}, \tag{12}$$

where $N_\gamma(E_{bin})$ is the integrated number of photons on target in a given tagger energy bin, ρ_D=0.169 g/cm^2 [2] is the density of liquid deuterium, $L_T = 40$ cm is the length of the target, $N_A= 6.02 \times 10^{23}$ deuterons/mol is Avogadro's number [2], and A_D=2.014 g/mol is the molar mass of deuterium. For the analyzed runs this number is approximately 25 pb^{-1} for the photon energy range between 4.5 GeV and 5.5 GeV.

The number of photons per energy bin is obtained from *gflux*, which is already corrected for the detector livetime. Therefore, the number of events in the data sample does not need to be corrected for the detector deadtime. The tagger efficiency in the event reconstruction and *gflux* cancel out because the photon reconstruction algorithm in the two procedures is the same. Fig. 19 shows the number of the photons per energy bin corresponding to the data sample which was analyzed in this work. This analysis uses only the portion of the tagger in the trigger corresponding to 4.55 GeV $< E_\gamma <$ 5.5 GeV. The typical uncertainties reported by *gflux* package for a single energy bin is on the order of $\sim 2\%$.
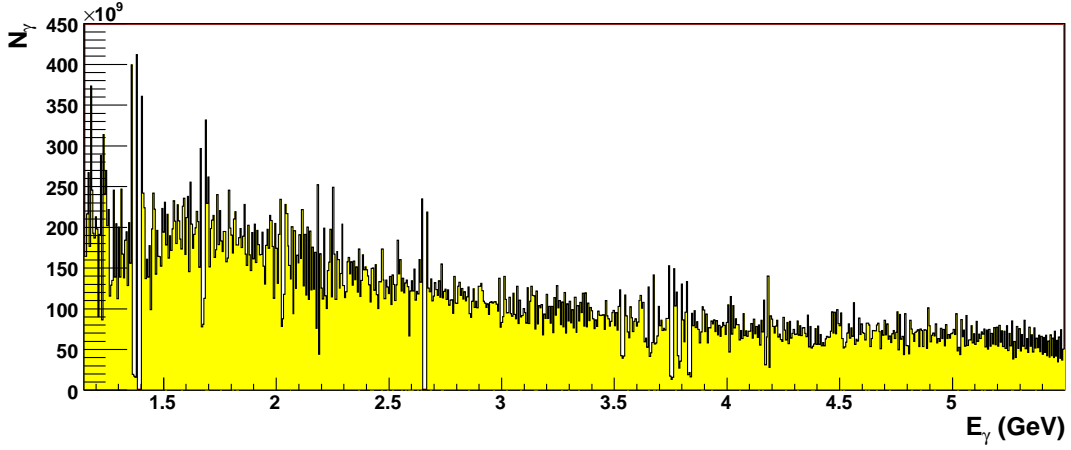
30

Figure 19: Number of photons per energy bin versus corresponding photon energy as determined by *gflux* package.

12 Systematics

The final spectrum for the invariant mass was studied for various values of the cut parameters for Λ, Ξ and π^- selection. These variations did not result in the qualitative change of the invariant spectrum of the invariant mass of $\Lambda\pi^-\pi^-$ or $\Xi^-\pi^-$ spectrum. In addition three independent parallel analysis, one of which included a kinematic fitting of the masses and vertexes of $\Lambda(1116)$ and $\Xi^-(1321)$, did not produce any statistically enhancements near mass $M = 1.860$ GeV.

We checked the sensitivity of the results with respect to the following parameters:

- selection parameters for the Λ-candidate in Eq. 2,

- DOCA cuts on the Λ and the Ξ^- candidates,

- $\widetilde{c\tau}$-cuts for $\Lambda(1116)$,

- PID cuts on β vs p,

- trigger simulation

- reaction model for $\Xi^-\pi^-$ production in the acceptance estimate.

31

The Λ-selection parameters choice, DOCA cut widths, $\widetilde{c\tau}$- and PID cuts did not affect the final result for the upper limit of the cross sections, and therefore we considered the uncertainties due to them negligible.

The dominant contribution to the photoproduction cross section systematic uncertainty is from the model dependence of the estimated acceptance value, and our simulation suggest $\sim 20\%$ relative uncertainty for the acceptance. All other systematic uncertainties in CLAS are typically under 10%, and therefore are neglected in this analysis, keeping in mind that the statisticall error bars for the raw data points are on the order of $\sim 20\%$.

During the offline analysis we noticed that the yields for four-track events in the three sector trigger were reduced by $\sim 20\%$ when the start counter was put in coincidence with the tagger Master OR signal before it was sent to the asynchronous trigger input of the CLAS trigger superwiser. This effect was accounted for by scaling the yields up by 16%, after taking into account the amount of time such a configuration of the trigger was used. An additional systematic uncertainty of 10% was assigned to the normalization.

The correctness of the upper limit extraction method has been verified by using two different approaches, which yielded consistent results, and are described in Sec. 15.1.3.

13 Invariant mass spectrum for $\Lambda\pi^-\pi^-$ system

Once the Λ is identified we select only the events which contain at least two negative pions. For these events we construct the invariant mass of $\Lambda\pi^-$ either using the "Liberal selection" or the "Conservative selection" methods. The mass spectrum using "liberal" method with $\widetilde{c\tau} > 1.5$ `cm` cut shown on on Fig. 9 a exhibits sharper peak than one in the Fig. 12 containing all $\Lambda\pi^-$ combinations with fiducial cuts, good run selection and photon matching in the tagger, but no $\widetilde{c\tau}$ cut ("conservative selection").

By applying the mass cut from Table 2 around the Ξ^--peak in Fig. 9 a we can construct the invariant mass of $\Lambda\pi^-\pi^-$ system, shown in Fig. 20. The spectrum does not exhibit any statistically significant enhancement near $M_{\Lambda\pi\pi} = 1.860\,\text{GeV}$. The spectrum contains $\Xi^-\pi^-$ events as well as non-cascade events. Therefore it is desirable to subtract the contribution of the non-cascade events to the $\Lambda\pi^-\pi^-$ mass spectrum, thus obtaining the $\Xi^-\pi^-$
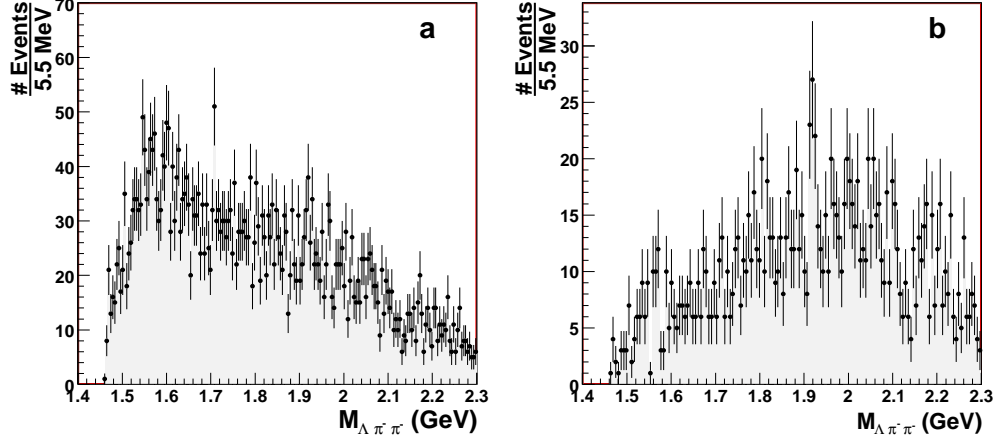
Figure 20: Invariant mass spectrum of $\Lambda\pi^-\pi^-$ system with "liberal selection" and $\widetilde{c\tau} > 1.5$ cm with (a) and without (b) requirement for an extra K^+. There is no statistically significant enhancement near mass $M = 1.860$ GeV.

invariant mass spectrum.

14 Invariant mass spectrum for $\Xi^-\pi^-$ system

The spectrum of interest for this analysis is of the invariant mass of $\Xi^-\pi^-$ system, which we obtain from the data sample with "Conservative Selection" of events. There are at least two different ways to obtain this spectrum. The first method is to select events containing $\Lambda\pi^-\pi^-$ system, put a tight cut around $\Xi(1321)$ peak, as described in Table 3, and from the $\Lambda\pi^-\pi^-$ mass spectrum of the selected events subtract the backround evaluated using sideband subtraction method. Alternatively, one can first bin all events in $\Lambda\pi^-\pi^-$ mass, and for each bin perform a fit in $\Lambda\pi^-$ to extract the $\Xi^-\pi^-$ yields.

14.1 Sideband Subtraction

We consider this method our main method of obtaining $\Xi^-\pi^-$ mass spectrum. Again, we put a cut around $\Xi(1321)$ peak (see Table 3) and combine $\Lambda\pi^-$ with another π^-, and plot the invariant mass of $\Lambda\pi^-\pi^-$ system, shown on Fig. 21 a. To account for the background non-cascade background we select
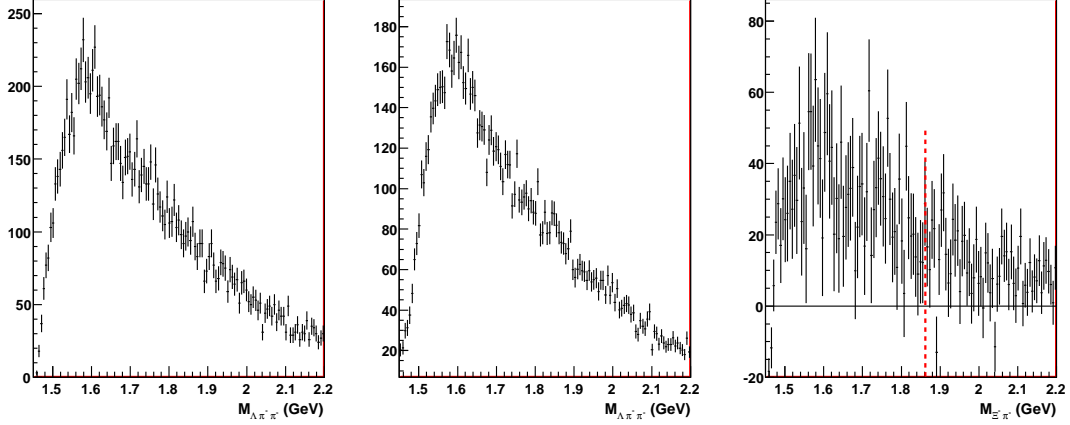
Figure 21: Invariant mass distribution of $\Lambda\pi^-\pi^-$ system with "conservative selection". The spectrum for all events under the Ξ^- peak are shown in panel (a); number of events from the left and right sidebands normalized to the background under the Ξ^- peak is in panel (b), and the sideband subtracted spectrum in panel (c).

sidebands from the left and the right sides of the $\Xi^-(3121)$ peak and use those events to subtract the background contribution in the $\Lambda\pi^-\pi^-$ mass spectrum. We chose the sidebands to be in the mass ranges of 1.300 GeV $< M_{\Lambda\pi^-\pi^-} <$ 1.310 GeV for the left sideband, and 1.335 GeV $< M_{\Lambda\pi^-\pi^-} <$ 1.345 GeV for the right sideband. The $\Lambda\pi^-\pi^-$ mass spectrum of the events from the two sidebands, Fig. 21 b, is normalized to the number of background events underneath the cascade peak. The subtracted mass dependence is shown on Fig. 21 c. There is no statistically significant enhancement near mass $M_{\Xi\pi} = 1.860$ GeV.

This procedure was performed for different cuts on $\widetilde{c\tau}[\Xi]$ to check for presence of any statistically significant enhancement near 1.862 GeV in the sideband-subtracted spectrum. None of the plots for $\Xi^-\pi^-$ invariant mass , shown in Fig. 22, exhibited any peaking near that mass range.

14.2 Cross-check with Fitting method

To cross check the sidebandband subtraction method we also extracted the yields of $\Xi^-\pi^-$ events in each $\Lambda\pi^-\pi^-$ mass bin by fitting the $\Lambda\pi^-$ mass
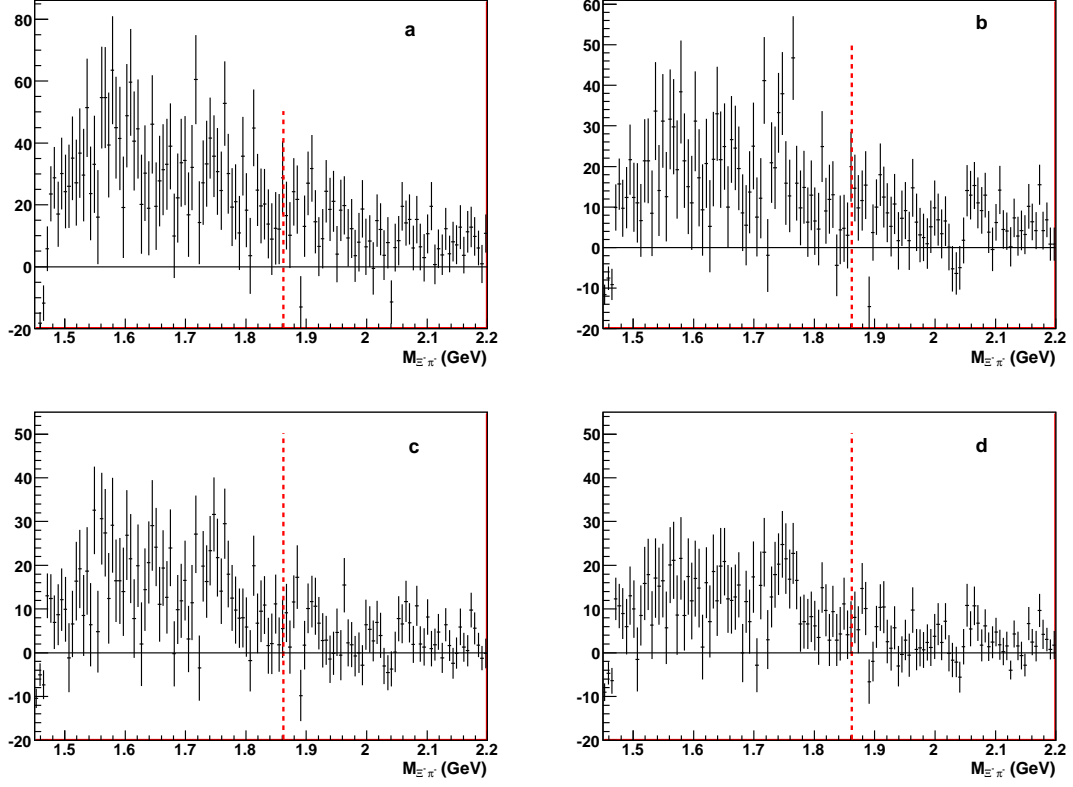
34

Figure 22: Invariant mass distribution of $\Xi^-\pi^-$ system with "conservative selection" four different $\widetilde{c\tau}$ cuts: a) $\widetilde{c\tau} > -25$ cm; b) $\widetilde{c\tau} > 0$ cm; c) $\widetilde{c\tau} > 1.5$ cm; d) $\widetilde{c\tau} > 2.5$ cm.
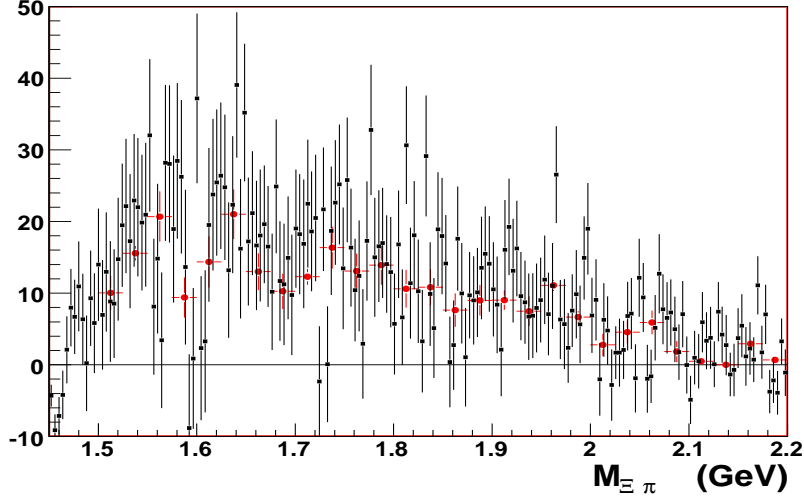
Figure 23: Comparison of the results for $\Xi^-\pi^-$ yields versus the invariant mass of the system. The red marker shows the result of the fitting method, while the black markers show the result of the sideband subtraction method. The yields from the sideband subtraction method is scaled by the ratio of the bin widths.

and $\widetilde{c\tau}[\Xi]$ distributions. Instead of fitting one dimensional histograms with a fixed $\widetilde{c\tau}[\Xi]$ cut we performed a two-dimensional fit with one axis defined by $\Lambda\pi^-$ mass, and the other axis by $\widetilde{c\tau}[\Xi]$. The model for the fit assumed Gaussian distribution for the $\widetilde{c\tau}[\Xi]$ and Breit-Wigner for invariant mass for events from $\Sigma^-(1385)$ decays. The events from $\Xi^-(1321)$ decays are assumed to be distributed according to a convolution of a Gaussian and exponential in $\widetilde{c\tau}[\Xi]$, and to a Gaussian in invariant mass. The "unknown" background is parametrized in form of two polynomials in $\Lambda\pi^-$ mass terms: first term is Gaussian in $\widetilde{c\tau}[\Xi]$, the second term behaves as a convolution of a Gaussian and exponential. The fitting procedure uses maximum likelihood method [35] because of the limited number of events in each $\Lambda\pi^-\pi^-$ mass bin. The comparison of the results from the sideband subtracted method and fitting method is shown in Fig. 23. The bin sizes in this plot are chosen wider than in Fig. 21 c, $\Delta M = 20$ MeV because we need a reasonable population in each $\Lambda\pi^-\pi^-$ mass bin to perform a fit. One can see that the two methods provide consistent results. Because the required binning for this procedure was too crude we did not use this method to obtain our final results. This method was

only used for cross-checking the the sideband subtraction procedure, which is our main method for extracting the $\Xi^-\pi^-$ yields.

15 Upper Limits

In order to extract the upper limits for the number of events and the photoproduction cross sections we utilized statistical analysis method similar to one describe in Ref. [36]. The cases described in Ref. [36] had already been implemented in the ROOT framework [28]. This method allows us to estimate the confidence belt for predetermined confidence level for models containing various nuisance parameters with their uncertainties. In this case these parameters are the background and acceptance/efficiency. For specified number of total observed events, estimated number of background events, the error for the estimated number of background events, acceptance/efficiency of the detector, and the uncertainty for the acceptance/efficiency, this method gives the corresponding confidence belt at a given confidence level (CL). As you will see from the sections below, we estimate that the upper limit for photoproduction cross section for $\Phi^{--} \rightarrow \Xi^-\pi^-$ in the energy range 4.5 GeV $< E_\gamma <$ 5.5 GeV in a mass window of 20 MeV at 90% confidence level is $\sim$ 450 pb.

15.1 Methods to estimate the upper limits

To estimate the upper limit we scan through the bins of the mass-dependent histogram. For each bin in the spectrum of the invariant mass of the $\Lambda\pi^-\pi^-$ system we select a 20 MeV wide window centered at that bin, and determine the upper limit of the excess events over the background. To estimate the number of background events we fit the histogram in Fig. 20 or Fig. 21 c with a smooth polynomial plus a Gaussian. The center of the Gaussian is fixed at the center of the bin, while the width of the Gaussian distribution is fixed at 7 MeV. Our studies show that the result practically does not depend on the choice of the width of the Gaussian. In fact, we get similar results even if we only use a polynomial function without Gaussian to estimate the background. The procedure to determine the acceptance/efficiency of the detection and reconstruction in CLAS is described in Sec. 10. In order to test the upper limit extraction procedure we performed a cross check with three methods. Our main method for obtaining the upper limits is the Rolke

method with Gaussian signal described in Sec. 15.1.2. For clarity we start by describing the Rolke method with Poisson distribution for total number of events from Ref. [36].

15.1.1 Rolke Method with Poisson Statistics

The first method is one of the models described in details in Ref. [36]. Working with the unsubtracted histogram in Fig. 20, using the total number of events in the window, the background, the acceptance and their uncertainties we can obtain the upper limit for the number of events using a Poisson model for the total number of events with Gaussian background and acceptance distributions using standart ROOT method. But for comparison here we ignore the acceptance and background uncertainties and assume 100% acceptance/efficiency. The reason for this is that one of the three methods described below is not well suited to handle acceptance and background uncertainties. The dependence of the upper limit at 90% confidence level for the number of the Φ^{--} events versus invariant mass of $\Lambda\pi^-\pi^-$ system with this method is shown with blue line on Fig. 24.

15.1.2 Rolke Method with Gaussian Statistics

The second method uses the sideband-subtracted histogram in Fig. 21 c. In this case the number of events is distributed according to Gaussian distribution because after subtracting the non-cascade background contribution the number of events and its variance are not related by $D(N) = \frac{1}{N}$ as it is in the case of binomial distribution. Here, the model for the excess of the events above the background is modeled by a Gaussian, limited by $\mu \geq 0$ condition since the cross section cannot be negative even if the number of observed events is less than the expected background.

The model includes efficiency for the true events distributed as a Gaussian, acceptance/efficiency distributed as a Gaussian, and the total observed number of events distributed like a Gaussian:

$$P(x, b_m, e_m \mid \mu, b, e) = \frac{1}{\sqrt{2\pi}\sigma_x} e^{-\frac{(e*\mu+b-x)^2}{2\sigma_x^2}} \times \tag{13}$$

$$\times \frac{1}{\sqrt{2\pi}\sigma_b} e^{-\frac{(b_m-b)^2}{2\sigma_b^2}} \times \frac{1}{\sqrt{2\pi}\sigma_e} e^{-\frac{(e_m-e)^2}{2\sigma_e^2}} ,$$

where μ is the number of the true events, e is the acceptance/efficiency factor

38
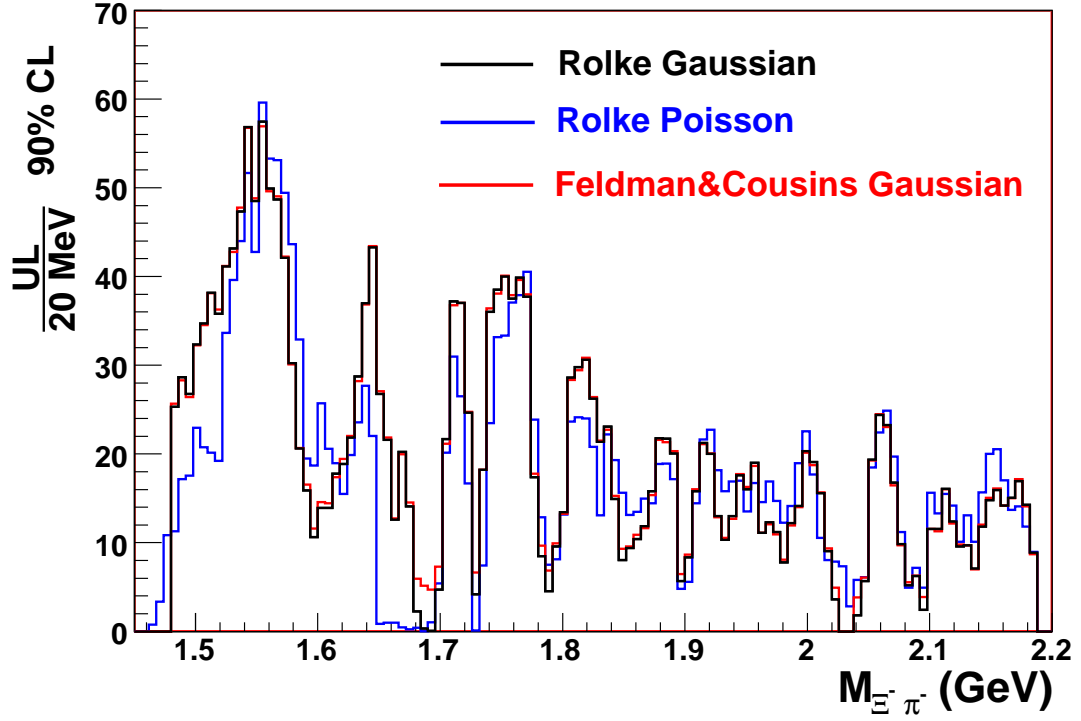
Figure 24: Upper limits for the number of events in 20 MeV window at 90% confidence level versus the mass of $\Lambda\pi^-\pi^-$ system. The black line shows the upper limit from sideband-subtracted histogram using Rolke method with Gaussian signal. The red line shows the upper limits from sideband-subtracted histogram using Feldman-Cousins method. The blue line shows the upper limits from unsubtracted histogram using Rolke method with Poisson model for the total number of events in the window.

for true events, b is the true background event number, x is the observed number of events, b_m is the estimated number of background events, e_m is the estimated acceptance/efficiency for true events. Rolke's method uses profile likelihood to estimate the confidence level. The profile likelihood is defined as the ratio of two likelihoods:

$$\lambda(\mu_t) \;=\; \frac{sup\{P(x, b_m, e_m \mid \mu_t, b, e); b, e\}}{sup\{P(x, b_m, e_m \mid \mu, b, e); \mu, b, e\}} \;= \tag{14}$$

$$=\; e^{-\frac{1}{2}\frac{(\mu_t e_m + b_m - x)^2}{\sigma_x^2 + \mu_t^2 \sigma_e^2 + \sigma_b^2}} \;,$$

where μ_t is the hypothesis being tested. The supremum in the denominator is taken over all values of (μ, b, e), while the supremum in the numerator is taken only over background and efficiency b, e. In the statistics the $-2\log\lambda(\mu_t)$ is approximated by the χ^2-distribution with the appropriate degrees of freedom (in our case there is one degree of freedom). Then if we need to find values of μ_t which correspond to certain Confidence Level (CL), we find the χ^2 value corresponding to that CL, and then find the values of μ_t where the values of the $2\log\lambda(\mu_t)$ are offset from its maximum value by that amount of χ^2. The first solution to the left side of the most likely value of μ will be the lower limit, and the one on the right would be the upper limit. The two solutions are:

$$\mu_b \;=\; \frac{-b_m\, e_m + x e_m}{e_m^2 + \chi^2 \sigma_e^2} \times \left(-e_m^2\, \chi^2 \sigma_x^2 - e_m^2 \chi^2 \sigma_b^2 + \right. \tag{15}$$

$$+\; 2\chi^2 \sigma_e^2 x b_m - \chi^2 \sigma_e^2 x^2 - \chi^4 \sigma_e^2 \sigma_x^2 - \chi^2 \sigma_e^2 b_m^2 - \left. \chi^4 \sigma_e^2 \sigma_b^2 \right)^{\frac{1}{2}} \times$$

$$\times\; \left(e_m^2 + \chi^2 \sigma_e^2\right)^{-1} \;.$$

The illustration of how the upper and lower limits are found is shown in Fig. 25. The red curve is $2\log\lambda(\mu_t)$ log-likelyhood function peaking somewhere around ~ -1400, which is the most likely value for the illustrated example. The probability of having 90% of the times within a certain range is realized at $\chi^2 = 2.705$, which is represented by the green line in Fig. 25. The intersection points of these curves are the upper and lower limits at 90% confidence level. In certain cases, for instance when the estimated efficiency is very low, and the uncertainty for it is relative large, then we can have cases when no upper or lower limits can be found. This happens because the profile likelihood does not look like a parabola, as it is in Fig. 25, but distorted and is not well approximated by the ξ^2-distribution.
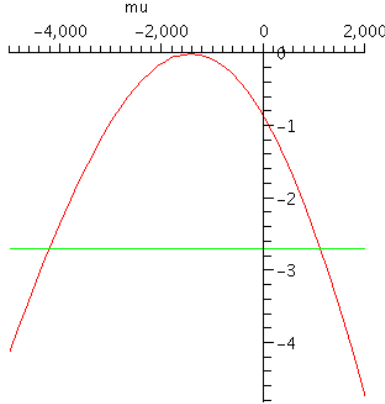
40

Figure 25: Illustration of determining the upper and lower limits for $CL = 90\%$. The x-axis is the expectation value for measured quantity μ. The red curve is the profile likelihood versus μ, and the green line is $\chi^2 = 2.705$.

In cases where the most likely μ_t is negative, we take lower limit to be 0. If the most likely μ_t is so negative that the upper limit is negative as well, we increment the number of observed events by one unit we get the first positive value. This adhoc adjustments can change the coverage, therefore one needs to check if the results obtained by this procedure provide desired confidence level. The Monte-Carlo tests showed that the error of the coverage is within 5%.

15.1.3 Feldman-Cousins method

In addition to the Rolke method [36] we performed a cross-check of our upper limit results for the total number of events using Feldman-Cousins method [37] used in previous CLAS pentaquark analyses. We used the Feldman-Cousins method for the case of the Gaussian distribution for the signal with boundary limit on expectation value $\mu \geq 0$ as described in Ref. [38]. A comparison of the three methods is shown in Fig. 24, where Feldman-Cousins method is represented by the red curve. As in the two previous cases the acceptance/efficiency is set to be 1, and zero background and acceptance uncertainty is assumed. Overall, the three methods are in good agreement,
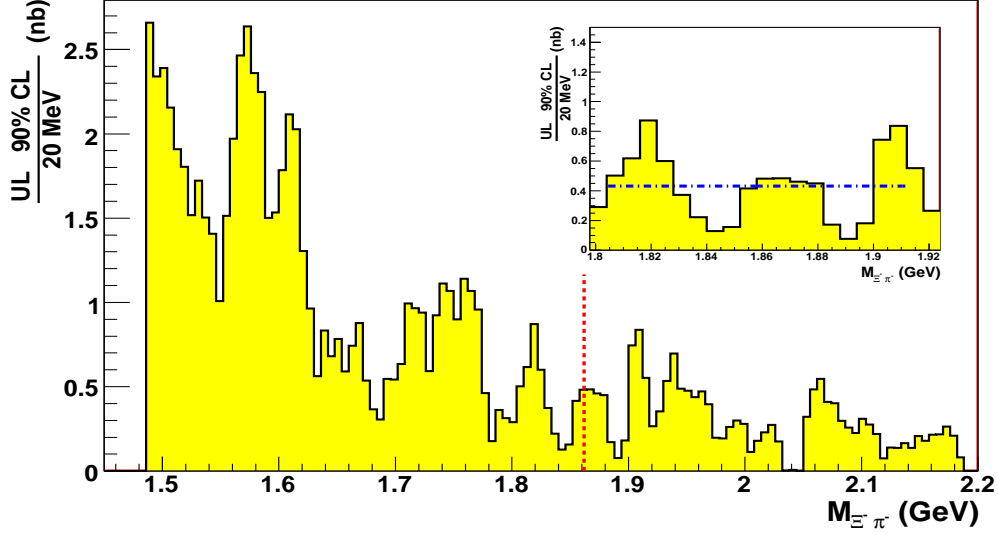
Figure 26: Upper limits for the photoproduction cross section in 20 MeV window at 90% confidence level versus the mass of $\Xi^-\pi^-$ system. The red dashed line shows where the expected position of the enhancement from the NA49 experiment. The horizontal blue dash-dotted line shows the averaged upper limit $UL = 0.43$ nb.

but there is relatively small discrepancies between the unsubtracted and subtracted methods in the mass range under $M < 1.75$ GeV. These differences can be explained by the fact that subtraction of sidebands introduces additional statistical uncertainty, therefore the upper limit estimates do not have to be identical before and after subtraction.

15.2 Upper limits for cross sections

In order to obtain the upper limit for the photoproduction cross sections for a mass window of 20 MeV we have to divide the number of events by the integrated luminosity. The uncertainty in the luminosity determination is negligible, on the order of $\sim 2\%$, compared to the model dependence of the acceptance calculation described in Sec. 10. The procedure for determining the luminosity is described in Sec. 11. Here we apply our method with Gaussian model for the excess of events using the sideband-subtracted histogram in Fig. 21 c. This time we use the real estimated acceptance and

the realistic uncertainties in the acceptance, the trigger efficiency and the background. Fig. 26 shows the upper limit for the cross section using the sideband-subtracted histogram versus invariant mass of $\Xi^-\pi^-$. The events in these plots were selected to have a matching photon in the energy range 4.55 GeV$< E_\gamma < 5.5$ GeV. The upper limit for the cross section in the mass range of 1.80 GeV$< M_{\Xi\pi} < 1.92$ GeV at these photon energies is ~ 450 pb.

16 Conclusions

We analyzed the entire EG3 data set to look for the $\Phi^{--}(1862)$ pentaquark candidate in the $\Phi^{--}(1862) \to \Xi^-\pi^-$ decay channel. The raw event spectrum does not show any statistically significant enhancement near the mass $M_{\Lambda\pi^-\pi^-} = 1.862$ GeV, neither does the sideband-subtracted spectrum. The upper limit for photoproduction cross section versus invariant mass of the $\Xi^-\pi^-$ was obtained using method similar to one described in Ref. [36]. On average the upper limit for the cross sections for Φ^{--} photoproduction near the threshold with subsequent decay $\Phi^{--} \to \Xi^-\pi^-$ at 90% confidence level for 20 MeV mass window averaged over the mass range of 1.80 GeV$< M_{\Xi\pi} < 1.92$ GeV is ~ 450 pb. This is an improvement of factor of four over the previously estimated upper limit from HERMES collaboration of ~ 2 nb [5].

A   Appendix

A.1   Good Runs

45552	45553	45554	45555	45556	45557	45558	45563	45566	45568
45569	45570	45571	45572	45576	45577	45578	45579	45580	45581
45582	45598	45599	45600	45601	45602	45603	45605	45606	45607
45608	45609	45612	45613	45614	45621	45622	45623	45624	45625
45626	45627	45804	45807	45808	45809	45810	45811	45812	45814
45815	45816	45817	45818	45847	45848	45851	45852	45860	45862
45863	45864	45866	45868	45869	45870	45872	45873	45874	45876
45891	45893	45894	45895	45896	45897	45902	45903	45904	45905
45906	45907	45911	45912	45913	45914	45916	45917	45918	45919
45920	45921	45922	45923	45924	45925	45926	45927	45928	45929
45930	45931	45932	45933	45934	45935	45936	45937	45938	45939
45942	45943	45944	45945	45946	45947	45948	45976	45977	45978
45981	45983	45984	45985	45986	45987	45988	45993	45995	45996
46000	46001	46002	46003	46004	46005	46009	46011	46012	46013
46014	46015	46016	46017	46018	46019	46020	46021	46022	46023
46024	46025	46028	46029	46030	46035	46036	46037	46038	46046
46047	46057	46058	46062	46063	46064	46065	46066	46069	46071
46072	46073	46074	46077	46078	46085	46086	46087	46088	46089
46093	46094	46096	46097	46098	46099	46100	46101	46104	46113

Table 7: Table of the CLAS runs used in this analysis.

References

[1] D. Diakonov, V. Petrov, and M. Polyakov. Exotic Anti-Decuplet of Baryons: Prediction from Chiral Solitons. *Z. Phys. A*, 359:305, 1997. [hep-ph/9703373].

[2] W. M. Yao et al. Review of particle physics. *J. Phys.*, G33:1–1232, 2006.

[3] C. Alt et al. (NA49 Collaboration). Observation of an Exotic S = -2, Q = -2 Baryon Resonance in Proton-Proton Collisions at the CERN SPS. *Phys. Rev. Lett.*, 92:042003, 2004. [hep-ex/0310014].

[4] M. I. Adamovich et al. Search for the exotic xgr –(1860) resonance in 340 gev c sigma –nucleus interactions. *Phys. Rev.*, C70:022201, 2004.

[5] A. Airapetian et al. Search for an exotic s = -2, q = -2 baryon resonance at a mass near 1862-mev in quasi-real photoproduction. *Phys. Rev.*, D71:032004, 2005.

[6] S. Chekanov et al. Search for pentaquarks decaying to xi pi in deep inelastic scattering at hera. *Phys. Lett.*, B610:212–224, 2005.

[7] E. S. Ageev et al. Search for the phi(1860) pentaquark at compass. *Eur. Phys. J.*, C41:469–474, 2005.

[8] K. T. Knopfle, M. Zavertyaev, and T. Zivko. Search for theta+ and xi(3/2)– pentaquarks in hera-b. *J. Phys.*, G30:S1363–S1366, 2004.

[9] B. Aubert et al. Search for strange-pentaquark production in e^+e^- annihilation at $\sqrt{s}$ = 10.58 gev. *Phys. Rev. Lett.*, 95:042002, 2005.

[10] Kevin Stenson. Pentaquark searches at focus. *Int. J. Mod. Phys.*, A20:3745–3748, 2005.

[11] A. Abulencia et al. Search for exotic s = -2 baryons in p anti-p collisions at s**(1/2) = 1.96-tev. *Phys. Rev.*, D75:032003, 2007.

[12] S. Schael et al. Search for pentaquark states in z decays. *Phys. Lett.*, B599:1–16, 2004.

[13] P. Achard et al. Study of inclusive strange-baryon production and search for pentaquarks in two-photon collisions at lep. *Eur. Phys. J.*, C49:395–410, 2007.

[14] A. Aktas et al. Search for baryonic resonances decaying to xi pi in deep-inelastic scattering at hera. 0400. DESY 07-045.

[15] B. A. Mecking et al. The cebaf large acceptance spectrometer (clas). *Nucl. Instrum. Meth.*, A503:513–553, 2003.

[16] D. Diakonov and V. Petrov. Where are the missing members of the baryon antidecuplet? *Phys. Rev. D*, 69:094011, 2004. [hep-ph/0310212].

[17] John R. Ellis, Marek Karliner, and Michal Praszalowicz. Chiral-soliton predictions for exotic baryons. *JHEP*, 05:002, 2004.

[18] Robert L. Jaffe and Frank Wilczek. Diquarks and exotic spectroscopy. *Phys. Rev. Lett.*, 91:232003, 2003.

[19] Robert Jaffe and Frank Wilczek. Systematics of exotic cascade decays. *Phys. Rev.*, D69:114017, 2004.

[20] Swarup Kumar Majee and Amitava Raychaudhuri. SU(6), Triquark states, and the pentaquark. *Phys. Rev.*, D77:074016, 2008.

[21] Marek Karliner and Harry J. Lipkin. A Diquark-Triquark Model for the KN Pentaquark. *Phys. Lett.*, B575:249–255, 2003.

[22] W. Liu and C.M. Ko. Photoproduction of Pentaquark Cascades from Nucleons. *Phys. Rev. C*, 69:045204, 2004. [nucl-th/0312119].

[23] W. Liu and C.M. Ko. Pentaquark Baryon Production in Nuclear Reactions. In *Nishiharima 2004, Pentaquark*, page 149. Talk given at the International Workshop on PENTAQUARK04, Spring-8, Hyogo, Japan, July 2004. [nucl-th/0410068].

[24] Yong-seok Oh, Hung chong Kim, and Su Houng Lee. Properties of baryon anti-decuplet. *Phys. Rev.*, D69:094009, 2004.

[25] R. A. Arndt, Yakov I. Azimov, M. V. Polyakov, I. I. Strakovsky, and R. L. Workman. Nonstrange and other unitarity partners of the exotic Theta+ baryon. *Phys. Rev.*, C69:035208, 2004.

[26] R. Gothe, H. Holtrop, E.S. Smith, and S. Stepanyan. Spokespersons for Search for "Exotic Cascades with CLAS Using an Untagged Virtual Photon Beam". JLab Experiment E-04-010, 2004.

[27] E. Blobel. The bos system for clas software. CLAS-NOTE 2007-016, 1995.

[28] R. Brun and F. Rademakers. Root: An object oriented data analysis framework. *Nucl. Instrum. Meth.*, A389:81–86, 1997.

[29] E. Pasyuk. Energy loss corrections for charged particles in clas. CLAS-NOTE 2007-016, 2007.

[30] Paul Mattione. Kinematic fitting of detached vertices. JLAB-PHY-07-643, May 2007.

[31] Stepan Stepanyan. Fsgen phase space generator. Private Communications.

[32] Maurik Holtrop. Clas geant simulation. www.physics.unh.edu/maurik/gsim_info.shtml.

[33] Robert Feuerbach et al. Drift chamber alignment. CLAS-NOTE 1998-002, 1998.

[34] G. Mutchler, S. Taylor, and E. Smith. Clas tof scintillator positions. CLAS-NOTE 1998-008, 1998.

[35] G. Cowan. *Statistical Data Analysis*, chapter 6. Oxford Science Publication, 1998.

[36] Wolfgang A. Rolke, Angel M. Lopez, and Jan Conrad. Confidence intervals with frequentist treatment of statistical and systematic uncertainties. *Nucl. Instrum. Meth.*, A551:493–503, 2005.

[37] Gary J. Feldman and Robert D. Cousins. A unified approach to the classical statistical analysis of small signals. *Phys. Rev.*, D57:3873–3889, 1998.

[38] Elton Smith. Feldman-cousins method for gaussian statistics. CLAS-NOTE 2007-019, 2008.